Physics – Uspekhi **51** (9) 955 – 974 (2008)

CONFERENCES AND SYMPOSIA

PACS numbers: 01.10.Fv; 61.80.Jh, 64.70.Kb, 81.40.Wx;
05.10.Ln, **64.60. – i**, **75.40. – s**; **42.55. – f**, 42.60.By, **42.65. – k**

Equilibrium and highly nonequilibrium states of condensed matter (Scientific session of the Physical Sciences Division of the Russian Academy of Sciences, 21 April 2008)

V V Ovchinnikov; A K Murtazaev; E A Khazanov, A M Sergeev

DOI: 10.1070/PU2008v051n09ABEH006795

On 21 April 2008, a scientific session of the Physical Sciences Division of the Russian Academy of Sciences was held at the conference room of the Lebedev Physical Institute, RAS. The following talks were presented:

(1) **Ovchinnikov V V** (Institute of Electrophysics, RAS (UB), Ekaterinburg) "Radiation-dynamic effects. Potential for producing condensed media with unique properties and structural states";

(2) **Garnov S V** (Prokhorov General Physics Institute, RAS, Moscow) "Femtosecond laser plasma of multiply ionized gases";

(3) **Murtazaev A K** (Institute of Physics, Dagestan Scientific Center, RAS, Dagestan State University, Makhachkala) "Critical properties of frustrated spin systems on a stacked triangular lattice";

(4) **Khazanov E A, Sergeev A M** (Institute of Applied Physics, RAS, Nizhnii Novgorod) "Petawatt lasers based on optical parametric amplifiers: their state and prospects".

Summaries of talks 1, 3, and 4 are given below.

PACS numbers: 61.80.Jh, 64.70.Kb, 81.40.Wx
DOI: 10.1070/PU2008v051n09ABEH006609

Radiation-dynamic effects. Potential for producing condensed media with unique properties and structural states

V V Ovchinnikov

1. Introduction

For some aspects of solid state radiation physics — the 'low-dose effect' (the influence of ionizing radiation on the structure and properties of materials at an insignificant number of displacements per atom [1, 2]) and 'long-range effects'[1] arising during the irradiation of condensed media by heavy charged particle beams [3, 4] — classical models fail to provide convincing explanations. Nor, as is quite obvious, are generation processes due to the irradiation of Frenkel pairs, dislocations, and other defects of any help if taken alone because the long-range scales involved are often many times larger than the size of polycrystalline grains (whose boundaries serve as sinks or barriers for structural defects). The overwhelming majority of proposed long-range mechanisms neglect the response of the irradiated medium, even though this response can be of crucial importance in some cases.

In this talk, various aspects of the effect of ionizing radiation on a substance are briefly analyzed in relation to the above problems. It is argued that the *radiation-dynamic* (RD) effect of ionizing radiation on *metastable* media is of particular importance.

In real life, the distribution of defects that form in a material irradiated with particles heavier than electrons — such as reactor neutrons, fission fragments, and accelerated ions (with energies from $10^3 - 10^4$ eV to $10^7 - 10^8$ eV) — cannot be represented as a system of single Frenkel pairs uniformly distributed over the volume of the material (Fig. 1a), but is qualitatively different from this [5, 6] (Fig. 1b – d, 2a).

The primary atoms that neutrons knock out of lattice sites displace other atoms, and so on, thus producing one or more dense cascades[2] of atomic displacements (Fig. 1b). Each such cascade contains from hundreds to tens of thousands of the target material atoms, many of which (from several hundred to several tens of thousands) are knocked out of their lattice positions. As a cascade develops, all the atoms, including those not displaced from lattice sites, change their kinetic energy many times in collisions with neighboring atoms, until the so-called thermal spike forms (see Section 2.1).

Interactions involving nuclear excitations and reactions are relatively few and of little or no importance for the analysis that follows.

The stopping of fission fragments, accelerated ions, and fast recoil atoms in condensed matter is due not only to elastic collisions with the atoms of the target but also to some energy being inelastically transferred to the electron system for the excitation and ionization of atoms (inelastic losses).

As the fission fragments and high-energy ions are stopped, the share of inelastic losses decreases, with the result that the particles increasingly produce primary recoil atoms (typically with energies in the range $10^4 - 10^6$ keV). Each of these gives rise to one or more dense atomic

[1] Ion bombardment experiments have shown that changes in the material structure and properties occur at a depth several orders of magnitude grater than the projected ion range.

[2] The term 'dense' refers to a cascade that has no branches in it, such that all the atoms in a compact region participate in collisions.

Uspekhi Fizicheskikh Nauk **178** (9) 991 – 1011 (2008)
DOI: 10.3367/UFNr.0178.200809e.0991
Translated by E G Strel'chenko, E Yankovsky, and N A Raspopov; edited by A M Semikhatov

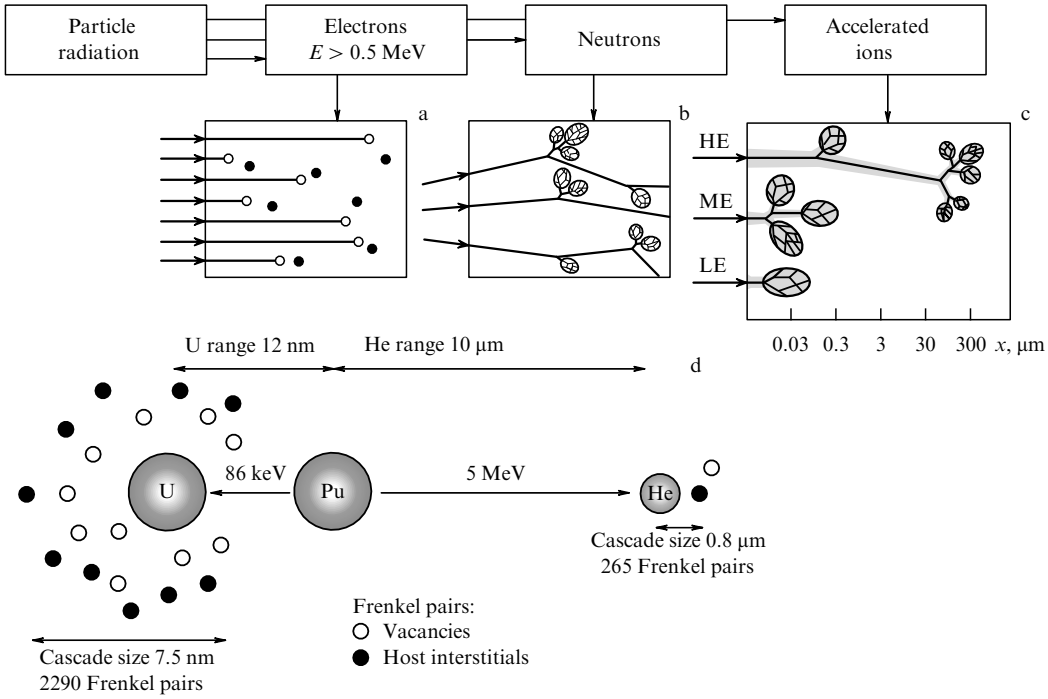

Figure 1. Damage types due to particle radiation: (a) electrons (single Frenkel pairs); (b) neutrons (passage zones for dense cascades of atomic displacements (i.e., depleted zones) are shown in Fig. 2a, e – h); (c) heavy ions and fission fragments (ionization and dense cascade regions); (d) dense cascade formation by a fission fragment in plutonium [7]. Panel c is a schematic not-to-scale diagram of high-energy (HE), medium-energy (ME), and low-energy (LE) ion radiation scenarios (a conventional classification is given in Ref. [8]).

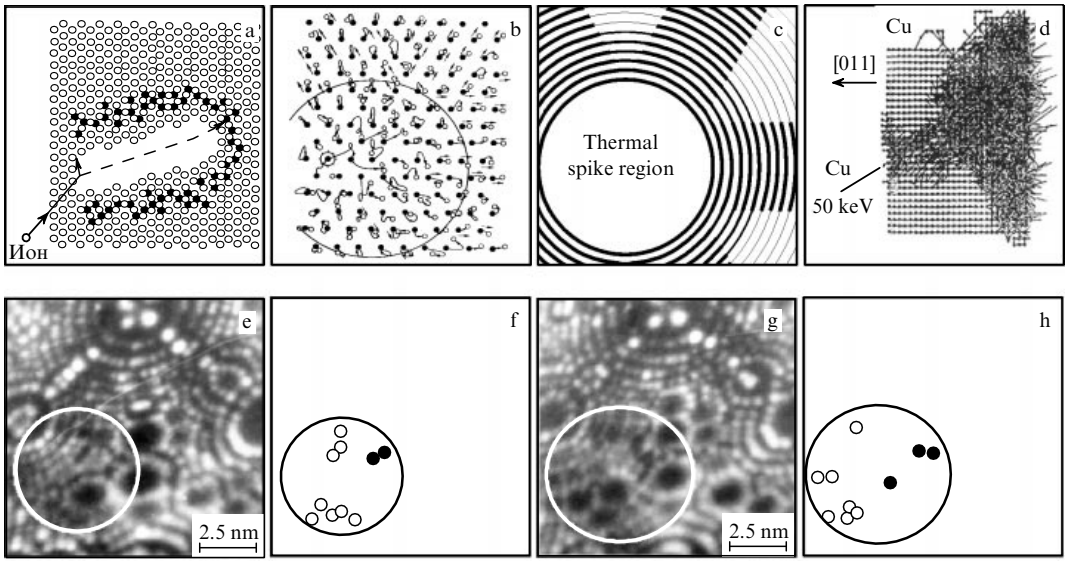

Figure 2. Structure and dynamics of radiation damage regions. (a) Schematic of the depleted zone emerging after the passage of an atomic displacement cascade [12]. (b) Results of a molecular dynamic modeling of a thermal spike [13]. (c) Schematic of how the focusing mechanism forms plane wave segments from the original spherical wave (see, e.g., Ref. [14]). (d) Development of a dense cascade: Cu → Cu (supercomputer modeling [15]). (e, g) Atomic resolution field-ion images of depleted zones in pure platinum irradiated by reactor neutrons with $E > 0.1$ MeV (the flux density 3.5×10^{22} cm^{-2}) [16]; the images in panels e and g are separated by two atomic layers (the atomic layers were removed one by one with an electric field). (f, h) The corresponding vacancy (white dots) and interstitial (black dots) distribution schematics.

displacement cascades, the same as with irradiation by reactor neutrons (Fig. 1c).

For low and medium-energy (1 – 100 keV [8]) ions, elastic and inelastic energy losses are comparable in value and mainly occur in the region of dense atomic displacement cascades. The reader is referred to Refs [8, 9] for estimates of the proportion of elastic and inelastic losses in a dense cascade. Other possible stopping mechanisms contribute negligibly at energies of interest here.

2. Radiation-dynamic effects due to particle irradiation

2.1 Post-cascade shock wave formation during the evolution of dense atomic collision cascades

As a cascade of atomic collisions develops, it takes about 10^{-12} s to 'thermalize,' i.e., to enter the 'thermal spike' state, in which the velocity distribution of the particles becomes Maxwellian [10]. (For comparison, the time scales of a chemical and a nuclear explosion are 10^{-5} and 10^{-8} s, respectively).

For a monoenergetic beam of heavy ions, the cascade region typically has the shape of an ellipsoid of rotation, if there are no channeling effects and the beam is normal to the surface of a flat target [9, 11] (Fig. 3a). Estimates for ions that are not very light are conveniently obtained by using the effective cascade radius R_0, which is taken to be equal to $\Delta R_\perp$, $\Delta R_\parallel$, or $(\Delta R_\parallel \Delta R_\perp^2)^{1/3}$ depending on the situation. For a dense cascade produced by an ion or a recoil atom with the energy $E > 10$ keV, the typical R_0 value is ~ 5 nm.

Favorably, even for metals, the time needed to remove heat from a region this size is sufficiently large, no less than 10^{-11} s according to Ref. [10], which exceeds the cascade thermalization time by at least an order of magnitude.

The maximum temperature of the cascade region can be estimated as the ratio of the energy E of a primary recoil atom (or an accelerated ion) to the number of atoms of the substance in the thermalized cascade.[3] This estimate agrees quite well with Monte Carlo simulations [10, 11] and experimental data [18, p. 90; 19]. For heavy ions, the maximum temperature of the cascade region can exceed 5000 – 6000 K. It is noteworthy that this temperature increases as the energy of the primary atom (or accelerated ion) decreases. The decisive factor here is how the volume of the cascade depends on energy (as the data in Ref. [19] confirm). Also, the cascade region can only be in a quasi-equilibrium state, which becomes increasingly nonequilibrium as the energy of the knocked out primary atom decreases and the cascade size decreases.

The energy release rate in dense cascades is nearly the same as in a nuclear explosion (with a nuclear plasma at $\sim 10^8$ K), although the specific energy release is more than 10^4 times lower.

The pressure limit in a cascade region, which can be estimated as $p = (E/V)(c_P/c_V - 1)$ [20, 21], is at least several tens of kilobars. When abruptly expanded, a strongly heated cascade region can produce a shock wave of a nearly spherical shape if the ions are not too light (Fig. 2b, 3a, b). Due to the operation of mechanisms that focus the wave energy into selected crystal directions [13 – 15], the transformation of the spherical wave into plane wave fragments is possible (Fig. 2b – d).

The primary recoil atoms for the reactor ion subsystem and heavy charged particles are most likely in the energy range between tens and hundreds of kiloelectronvolts and produce one or more dense atomic collision cascades over the length of their range ($\lesssim 1$ μm). Thus, the emergence of nanosize regions of explosive energy release with the emission of shock waves is common for various types of particle irradiation (except for particles less massive than nucleons).

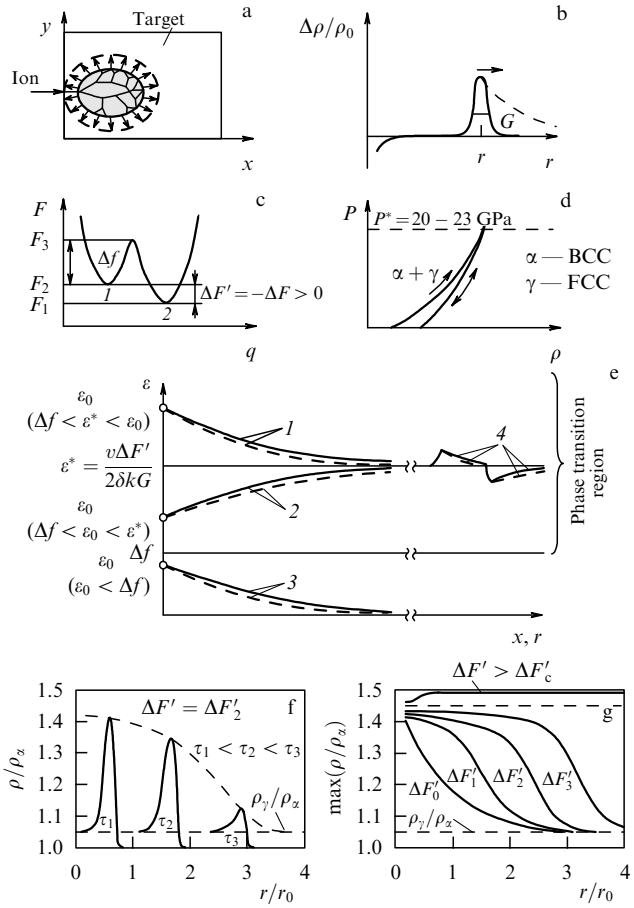

Figure 3. Schematic nature of radiation-dynamic structure – phase transformations. (a) Formation of a nanoshock wave at the final evolution stage of a dense atomic displacement cascade. (b) Profile of the post-cascade shock wave (relative change in the density of the medium) [22]. (c) Schematic change in the free energy of the system (*1*, metastable state; *2*, stable state). (d) Irreversible phase transition in the hydrostatically loaded $Fe_{69}Ni_{31}$ alloy. (e) The solution of the equation $d\varepsilon/d\xi = -2\beta\varepsilon + \Delta F'/(kG)$ for a plane wave (solid lines) and a spherical wave (dashed lines); lines *1*, *2* and *4* are an undamped, self-amplitude-modulated wave, *3* is a damped wave. (f, g) Numerical solutions of hydrodynamic equations; (e) the wave profile as a function of time; (g) atomic density change at the wave peak for different values of $\Delta F'_i$ ($\Delta F'_0 < \Delta F'_1 < \Delta F'_2 < \Delta F'_3$), an undamped phase-transition wave at $\Delta F' > \Delta F'_c$. BCC and FCC stand for bulk centered cubic and face centered cubic.

The same is true for the self-irradiation of fissioning materials (Fig. 1d), which is a process involving the aging of materials [7].

We note that until recently, the explosive energy release by emitting solitary shock waves has not been considered in studying the behavior of condensed matter, including media with high stored energy under irradiation conditions.

2.2 Propagation of post-cascade shock waves in stable media

The propagation of post-cascade shock waves in thermodynamically equilibrium (*stable*) media has been the subject of many studies, in particular, Refs [22 – 24]. According to some estimates (see Refs [22, 25]), the pressure at the front of a

[3] Strictly speaking, this is true only for dielectrics. In semiconductors and metals with few structural defects and a large electron mean free path, the energy (about $0.2E$ according to Ref. [8]) released in dense cascades into the electron subsystem (electron slowdown) is carried away from the dense cascade region [17] through the electron subsystem so fast that it has no time to be 'pumped' into the energy of neutrons.

post-cascade shock wave in the case of irradiation with heavy ions can exceed the yield strength limit of solids, not only the real (due to stresses of unblocked dislocations) but also the theoretical one. In the latter case, stresses at the front of a shock wave are sufficient for a defectless material to start to flow with mixing of atoms, giving rise to new dislocations and other defects behind the wave front. Following the region of increased pressure is an unloading wave [22].

The anomalous mass transfer [26] due to a large number of solitary shock waves can be an alternative to diffusive mass transfer. This process sharply increases the number of displacements per atom in the bulk of the material (see, e.g., Ref. [27]), although the temperature can be insufficient for the normal and radiation-enhanced diffusion to occur. The difference in pair-interaction energies w_{ij} for different atomic species under the conditions of a 'radiation-dynamic' material flow at the wave front can lead to a correlated rearrangement of atoms [21] and, ultimately, to the occurrence in a condensed medium of intraphase rearrangements and phase transformations [21, 27] that produce the short- and long-range atomic order normally controlled by diffusion processes.

As shown in Ref. [28], a shock wave can overcome the boundary of a grain, losing about 10 – 20% of its energy in the process.

Due to their high front pressures, post-cascade shock waves can also initiate diffusionless processes of the martensitic transformation type (some features of a diffusionless transformation initiated by ion irradiation can be seen in the inverse $\alpha \to \gamma$ transformation in the $Fe_{69}Ni_{31}$ alloy [29]; see also Section 4.1, Fig. 5a).

It is readily calculated that for $R_0 \sim 5-10$ nm, a spherical post-cascade wave in a stable medium travels at best several tens of nanometers before being damped tenfold, making it impossible to explain 'long-range effects' at distances of tens, hundreds, or even thousands of micrometers (see Section 4).

2.3 Theoretical model of self-sustained (self-propagating) radiation-induced structure – phase transformations in metastable media

The author and his colleagues studied [29, 30] post-cascade wave propagation in metastable media, that is, media that are not at the absolute (global) minimum of energy but at a certain intermediate, shallower local minimum separated from the former by an energy barrier Δf (Fig. 3c).

To overcome the energy barrier Δf requires either an energy fluctuation (after which, in a metastable medium, the process develops spontaneously with an energy release) or a sufficient external energy supply to a certain critical volume of the material (for example, following the radiation-induced formation of a thermal spike). The irradiation, ultimately leading to the emission of shock waves, serves as a triggering mechanism here.

Overcoming the potential barrier involves an energy release that exceeds Δf by the amount $\Delta F' = -\Delta F > 0$ (Fig. 3c). If the energy dissipation rate (i.e., the damping rate) of a wave propagating in a metastable medium does not exceed the energy release rate at the phase transformation front, then this wave is expected to become self-propagating.

In Ref. [29], the propagation of a hard-profile soliton wave in a metastable medium (Fig. 3b) is considered by replacing the usual damping equation $d\varepsilon/d\xi = -2\beta\varepsilon$ by the equation $d\varepsilon/d\xi = -2\beta\varepsilon + \Delta F'/(kG)$, which accounts for the energy release at the wave front driving the structure – phase transformation and in which ε is the energy at the wave profile maximum (per atom/molecule of the medium), $\xi = x$, $\beta = \delta/v$ for a plane wave and $\xi = r$, $\beta = \delta/v + 1/r$ for a spherical wave (x and r are the front coordinates, δ is the damping coefficient, and v is the wave velocity), and k and G are the shape factor and the half-height width of the wave profile (Fig. 3b) (for a Gaussian wave profile, $k = \sqrt{\pi/4\ln 2} \approx 1.06$ [29]). For a plane wave, the solution is given by

$$\varepsilon(x) = \begin{cases} \varepsilon_0 \exp\left[-\dfrac{2\delta(x-x_0)}{v}\right], & \varepsilon_0 < \Delta f, \\ \varepsilon^* - (\varepsilon^* - \varepsilon_0)\exp\left[-\dfrac{2\delta(x-x_0)}{v}\right], & \varepsilon_0 \geqslant \Delta f, \end{cases} \tag{1}$$

where $\varepsilon^* = \Delta F'/(2\delta kG)$.[4]

For $\varepsilon_0 < \Delta f$ (Fig. 3e), a usual damped wave is observed. The simultaneous conditions $\varepsilon_0 > \Delta f$ and $\varepsilon^* > \Delta f$ produce an amplitude-self-regulated wave (a wave that restores its amplitude when perturbed by medium inhomogeneities). For other relations between the control parameters ε_0, Δf, and ε^*, the solutions are also rather simple to analyze. Using the damping rate estimate obtained above for a spherical post-cascade wave in a stable medium (the corresponding range radius ~ 100 nm) and noting that the half-height profile width of a solitary wave is of the order of 1 nm according to Ref. [22], we easily estimate that the condition $\varepsilon^* > \Delta f$ is already satisfied at about $\Delta F'_{cr} > 0.02\Delta f$.

This means that a wave becomes undamped even if it is fed very little in the course of structure – phase transitions. It is only necessary that the energy of an accelerated particle that is released in the cascade region (per cascade atom: $E/N \geqslant \varepsilon_0$) be confidently larger than the energy required to do the work of overcoming the energy barrier Δf between the stable and metastable states, and that the characteristic size (radius) R_0 of the cascade significantly exceed the characteristic heat conduction length (to not give heat enough time to 'run away' from the cascade region before the cascade thermalizes and emits a shock wave):

$$\sqrt{\varkappa\tau} \ll R_0 < \left[\frac{E}{(4/3)\pi\rho\Delta f}\right]^{1/3}, \tag{2}$$

where τ is the cascade thermalization time, $\varkappa$ is the thermal diffusivity, and ρ is the atomic density of the material [cm^{-3}].

In Ref. [30], we treated this problem with a more rigorous hydrodynamic method based on the use of the Altshuler – Bushman – Fortov equation of state

$$\frac{\partial\rho}{\partial\tau} + \frac{\partial(\rho u)}{\partial r} + \frac{2}{r}\rho u = 0, \tag{3}$$

$$\frac{\partial u}{\partial\tau} + u\frac{\partial u}{\partial r} + \frac{1}{\rho}\frac{\partial p}{\partial r} = 0, \tag{4}$$

$$\frac{\partial\varepsilon}{\partial\tau} - \frac{p}{\rho^2}\frac{\partial p}{\partial\tau} = 0, \tag{5}$$

$$-\rho_\alpha c = \rho(u-c), \tag{6}$$

$$\rho_\alpha c^2 + p_0 = \rho(u-c)^2 + p + p_0, \tag{7}$$

$$\frac{1}{2}c^2 + \frac{\gamma_\alpha}{\gamma_\alpha - 1}\frac{p_0}{\rho_\alpha} + \Delta F' = \frac{1}{2}(u-c)^2 + \frac{\gamma_\gamma}{\gamma_\gamma - 1}\frac{p+p_0}{\rho} + \frac{\gamma_\gamma - 5/3}{2(\gamma_\gamma - 1)}\frac{p + p_0 - p_0(\rho/\rho_\gamma)^{\gamma_\gamma}}{\rho\Gamma_\gamma}, \quad \gamma_s = 2\Gamma_s + \frac{1}{3} \tag{8}$$

[4] The solution for a spherical wave is more complex but qualitatively similar.

(for notation, the reader is referred to Ref. [23], in which another version of the equation is given). Specifically, the problem was concerned with the alloy $Fe_{69}Ni_{31}$, in which we had previously observed [31–35] an inverse BCC (α) $\rightarrow$ FCC (γ) phase transformation initiated by 20 keV Ar^+ irradiation and terminating in several seconds of irradiation at a temperature lower than that for a similar thermal transformation (see Section 4.1, Fig. 5a).

It is known [36] that applying static pressure of the order of 20 GPa causes an irreversible BCC (α) $\rightarrow$ FCC (γ) transformation (Fig. 3d).

Importantly, the hydrodynamic equations were written by noting that the material properties experience a sudden jump at the transition from the BCC (α) to the FCC (γ) state:

$$\varepsilon = \varepsilon_s = \varepsilon^{B_0^s}_{\Gamma_s}(p,\rho)\,,$$

$$\varepsilon = \begin{cases} \varepsilon_\alpha = \varepsilon^{B_0^\alpha}_{\Gamma_\alpha}(p,\rho)\,, & \rho_0 = \rho_0^\alpha\,,\ B_0 = B_0^\alpha\,,\ \Gamma = \Gamma_\alpha \\ & \text{for } \alpha \text{ phase}\,, \\ \varepsilon_\gamma = \varepsilon^{B_0^\gamma}_{\Gamma_\gamma}(p,\rho)\,, & \rho_0 = \rho_0^\gamma\,,\ B_0 = B_0^\gamma\,,\ \Gamma = \Gamma_\gamma \\ & \text{for } \gamma \text{ phase} \end{cases},$$

$$\varepsilon = \frac{1}{\Gamma\rho}\left\{p - \frac{B_0}{2\Gamma+1/3}\left[\frac{\Gamma-2/3}{2\Gamma-2/3}\left(\frac{\rho}{\rho_0}\right)^{2\Gamma+1/3} - (\Gamma+1)\right]\right\}, \tag{10}$$

$$\varepsilon_\alpha = \varepsilon_\gamma + \Delta F'\,, \tag{11}$$

$$p = p_s = p^{B_0^s}_{\Gamma_s}(\rho)\,,$$

$$p = \begin{cases} p_\alpha = p^{B_0^\alpha}_{\Gamma_\alpha}(\rho) & \text{for } \alpha \text{ phase}\,, \\ p_\gamma = p^{B_0^\gamma}_{\Gamma_\gamma}(\rho) & \text{for } \gamma \text{ phase}\,, \end{cases} \tag{12}$$

$$p = \frac{B_0}{2\Gamma+1/3}\left[\left(\frac{\rho}{\rho_0}\right)^{2\Gamma+1/3} - 1\right], \tag{13}$$

where B_0 is the zero-temperature hydrostatic compression modulus, Γ is the Grueneisen constant, ρ is the atomic density, and $s = \alpha, \gamma$. The wave damping effect was taken into account by introducing the pseudoviscosity of the medium in accordance with the Neumann–Richtmyer equation [30].

The numerical solution of the above equations shows (see Fig. 3f, g) that as more energy is released at the wave front in the course of the phase transformation, a plateau develops and steadily expands on the wave-amplitude-versus-distance plot, and a regime where the transformation wave becomes undamped is entered for $\Delta F' > \Delta F'_c$. This, by and large, confirms the modeling results mentioned above concerning a hard-profile soliton wave propagating in a metastable medium.

3. Various types of radiation-dynamic transformations

Because of the extremely low diffusion rate of atoms at $T < T_c$, where T_c is a kind of threshold for 'defreezing' diffusion processes, some alloys can exhibit a hysteresis for direct and reverse structure–phase transitions (due to finite-rate heating and cooling, respectively) and allow a high-temperature state to be retained at lower temperatures by means of a fast quenching. At any temperature $T < T_c$, the alloy can be in either of two states, stable or metastable, depending on its past history.

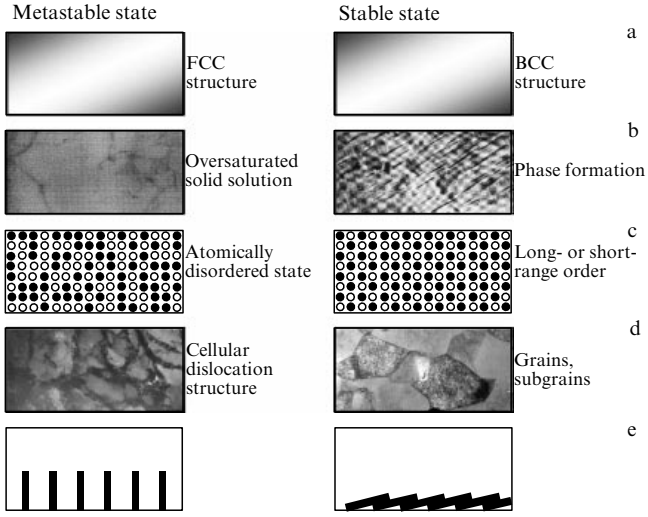

Figure 4. Examples of stable and unstable states at room temperature. (a) $Fe_{69}Ni_{31}$ alloy experiencing a BCC $\leftrightarrow$ FCC phase transformations ($\alpha \leftrightarrow \gamma$) on heating and cooling. (b) Oversaturated solid solutions Al–4% Cu (with heating-induced formation of Guinier–Preston zones, θ' and θ phases [37], and Fe–8% Mn (with formation of a γ phase) [38]. (c) Self-ordering alloys with a long-range (Fe–Al, Pd–Cu, Fe–Pd–Au) [27, 29, 32, 33, 39–41] and short-range (Fe–Cr, Fe–Si) [21, 42] atomic order. (d) Hardened and annealed industrial aluminum alloys [43–46] (the alloys shown are those in which, along with thermal annealing, the author and his colleagues observed *fast radiation annealing* at lowered temperatures). (e) Domino effect.

In Figs 4a–d, the stable and metastable states of metal alloys at room temperature are illustrated for alloys in which, in addition to thermal annealing, fast radiation annealing was observed by the author and coworkers at a lowered temperature (Fig. 4d).

If a system of N domino pieces (Fig. 4e) structured in a certain way is taken (as it can be) as a model for a metastable medium, then heating the medium into a stable state can be likened to simultaneously toppling N pieces and imparting N energy units to them (which corresponds to imparting energy to the entire volume of the substance). The triggering of a self-propagating process through the toppling of a single domino piece by imparting a single energy unit to it is analogous to a radiation-dynamic transformation.

4. Material treatment using radiation-induced effects

In all the experiments described below, we chose metastable media with increased stored energy as the objects affected by the action of accelerated ion beams (N^+, Ar^+, Fe^+, Cu^+).

In each experiment, the irradiation temperature was monitored and the observed effects were compared with those produced by a purely thermal influence (in the absence of irradiation) when the ion beam heating regime is exactly reproduced. In some cases, up to 100% of the ion beam power density was steadily replaced by light radiation such that the stationary temperature of the irradiation (and hence the intensity of thermostimulated processes) remained unchanged. The irradiation temperatures that were typically used were extremely low, much below the threshold for 'defreezing' diffusion (above the threshold, thermostimulated diffusive phase transformations occurring in very short times are already possible).

4.1 Modifying the resistive properties of alloys

In Figs 5a – b, results of the effect of accelerated ion beams on the resistive properties of the alloy systems Fe – Ni [29], Fe – Pd – Au [27, 29, 41], and Pd – Cu [39, 40] are presented and compared with those from a usual thermal treatment.

All three alloy systems share the feature that because of an RD component[5] in the particle (corpuscular) irradiation effect on a substance, the *metastable-to-stable* transition (see the caption to Figs 5a – c) has a much lower temperature threshold (by 50 to 165 K, depending on the alloy) compared to the thermostimulated transition.

For high-resistance $FePd_2Au$, a virtually zero temperature coefficient of electric resistivity (TCR) was achieved (Fig. 5b) due to a special type of a long-range order forming in the bulk of the material under the irradiation conditions [27, 41].

The reasons expounded in Section 2.2 underlie a sharp increase in the low-temperature mobility of atoms in the bulk of disordered alloys $FePd_2Au$ and $Pd_{45}Cu_{55}$ (in samples 100 μm thick studied) under their surface[6] irradiation by Ar^+ and Cu^+ ions (Fig. 5b, c) and, accordingly, a decrease in their ordering temperature when heated by an ion beam. This is confirmed by a detailed X-ray diffraction analysis [27, 39, 40].

The change in the electric resistance and TCR of the $Fe_{69}Ni_{31}$ alloy (Fig. 5a) can also occur because a short-range order forms on it at anomalously low temperatures.

That a phase transition is complete to a degree depending on the radiation dose can be due to the focusing effect of the vibration energy of the lattice [14], resulting in the initially spherical post-cascade wave transforming into plane-wave fragments (Fig. 2b – d). Another possible reason is that each separate post-cascade wave increases the degree of transformation only partially when it passes [27, 29].

4.2 Changing the magnetic properties of alloys

A major discovery is that radiation treatment strongly affects the magnetic properties of $Fe_{69}Ni_{31}$ [29, 32 – 34] and the atomic [42] and magnetic [47 – 49] structure and electrical engineering properties of transformer steels, permalloy, and amorphous and nanocrystalline magnetically soft materials (finemets).

The effect of the heating of a material concomitant to its irradiation by high-intensity ion beams was eliminated by using an intermittent or a low-frequency pulse-repetitive irradiation regime.

It was demonstrated in [32 – 34] that irradiation by N^+ and Ar^+ ions in a continuous or pulse-repetitive regime significantly affects (in a regime-dependent way) the superfine magnetic structure of the Mössbauer spectrum of the $Fe_{69}Ni_{31}$ alloy, presumably because ion irradiation accelerates atomic rearrangement processes and produces a short-range order within foils 30 μm thick. The foil temperature did not exceed 200 °C. Earlier, it was only at superhigh pressures that atomic nuclei showed a similar change in superfine magnetic fields in this alloy. The spectrum does not change shape if the material is heated in the usual way to the temperature 200 °C.

In Ref. [47], the damaging (formation of defects in a surface layer tens of nanometers thick) and the radiation-dynamic effects of accelerated ions were taken into consideration to optimize irradiation regimes for the formation in anisotropic transformer steel 3424 (Fe – 3% Si) of a special *atomic* structure [42], *defect* structure, and *magnetic domain* structure much finer than the original ones shown in Fig. 5d. With this radiation treatment, losses due to magnetization reversal in the working frequency range (400 – 5000 Hz) were reduced by 6% to 20% at the induction 1.5 T. The magnetic domain structure changes to a depth of 5 to 10 μm, several orders of magnitude larger than the projected range of accelerated Ar^+ ions.

The anisotropic steel improves its electrical engineering properties because of a complex combination of factors, such as an increase in the perfection of the alloy atomic structure due to the radiation-annealing-induced ordering [47] and the formation of a unique, multilayer magnetic domain structure consisting of narrow domains (Fig. 3d) perpendicular to the easy magnetization axis [001].

A detailed study [47, 48] of how amorphous ribbons of the $Fe_{73.5}Cu_1Nb_3Si_{13.5}B_9$ alloy change their electrical engineering properties when irradiated by beams of accelerated Ar^+ ions after first being subjected to standard finishing treatment (0.5 h annealing at 530 °C to provide a nanocrystalline structure and the best ribbon properties) enable an additional (on average) 10% reduction in remagnetization losses in the frequency range from 50 Hz to 10,000 Hz due to a more perfect structure obtained.

Importantly, a patent on the combined ion-beam/thermomagnetic treatment of permalloy (Fe – 70% Ni) and transformer steel (Fe – 3% Si) [50] was obtained. The radiation-dynamic influence of an accelerated ion beam prior to the thermomagnetic treatment results in the structure of these materials being deeply refined with respect to impurities and defects [49], thus improving their electrical engineering properties. The reduction in the coercitive force compared to the purely thermomagnetic treatment is 27%. An additional reduction in the loss due to magnetization reversal in transformer steel is about 15%.

4.3 Radiation annealing of industrial aluminum alloys

The Institute of Electrophysics, Ural Branch of the Russian Academy of Sciences, and the Kamensk-Uralsk Metallurgical Works (KUMW Corp. Ltd) joined the efforts in developing radiation annealing technologies in place of the furnace annealing of rolled aluminum products (a labor and energy-consuming industrial process used to remove cold work[7]) and looking for methods for improving the intermetallic composition and mechanical properties and other performance characteristics of finished products.

Detailed studies [43 – 46, 51] of the dislocation, grain, and intermetallic structure of cold-rolled aluminum products have allowed optimizing the regimes of the fast (a few seconds) radiation annealing of industrial aluminum alloys of various compositions and developing basic technologies for this process.

The practical results of the study, together with the radiation regimes, are presented in Table 1 and in Figs 5e and 5f.

In the most general and fundamental terms, these studies have shown that the radiation effects (in this case, ion

[5] In Refs [21, 38], the contribution of the RD effect was separated by replacing up to 100% of the ion beam power density by light radiation.

[6] In solids, the mean range of heavy accelerated 10 – 100 keV ions does not exceed 1 μm.

[7] 'Cold work' refers to an increase in internal stresses and strength of a material as it undergoes cold plastic deformation. This makes the material crack-prone and its further rolling impossible without intermediate furnace annealing at increased temperatures.

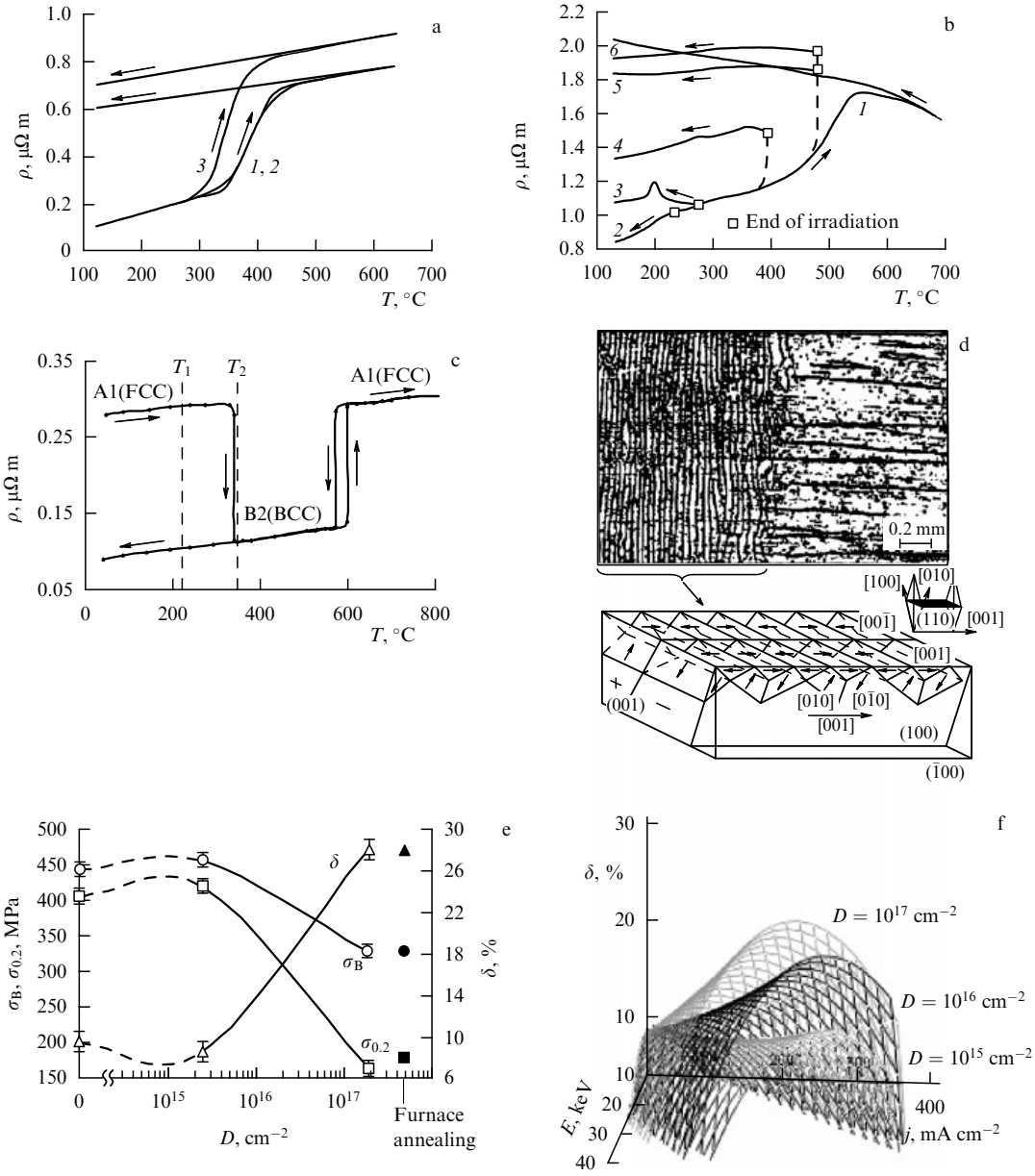

Figure 5. Examples of long-range RD effects and their radiation treatment applications. (a) Reduction in the phase transition temperature and changes in ρ and TCR for $Fe_{69}Ni_{31}$ (line *3*) irradiated by Ar^+ ions ($E = 20$ keV, $j = 80$ μA cm^{-2}) compared to the same for usual heating (lines *1*, *2*) [29]. (b) *In situ* electric resistance of the $FePd_2Au$ alloy disordered by quenching under heating and cooling (line *1*) and under irradiation (lines *2*–*6*) by Ar^+ ions ($E = 20$ keV, $j = 80$–100 μA cm^{-2}); the required irradiation temperatures were provided by using a heater and varying the ion current density. (c) Temperature of the A1 → B2 phase transition in the disordered $Pd_{45}Cu_{55}$ alloy under usual heating at 2 K min^{-1} (T_2) and under irradiation by Ar^+ ions (T_1) ($\Delta T = T_2 - T_1 = 135$ °C) [39]. (d) The magnetic domain structure and domain closure pattern in silicon iron Fe–3% Si upon irradiation by Ar^+ ions [40] (the right-hand part of the surface was masked from the irradiation; the arrows indicate domain magnetization directions). (e) Radiation and furnace annealing results for industrial alloy AMg6 (see Table 1) [43]. (f) Plasticity of the AMg6 alloy for various radiation annealing regimes.

Table 1. Mechanical properties of industrial sheets of AMg6, 1441, and BD1 aluminum alloys following thermal and radiation annealing.

Treatment	Alloy								
	AMg6			1441			BD1		
	σ_B, MPa	$\sigma_{0.2}$, MPa	δ, %	σ_B, MPa	$\sigma_{0.2}$, MPa	δ, %	σ_B, MPa	$\sigma_{0.2}$, MPa	δ, %
Cold deformation	445	407	9	315	296	3	255	246	6
Industrial annealing (2 h)	328	178	28	245	134	20	182	86	25
Radiation annealing by Ar^+ ions (5–30 s)	335	174	26	218	130	19	200	81	23

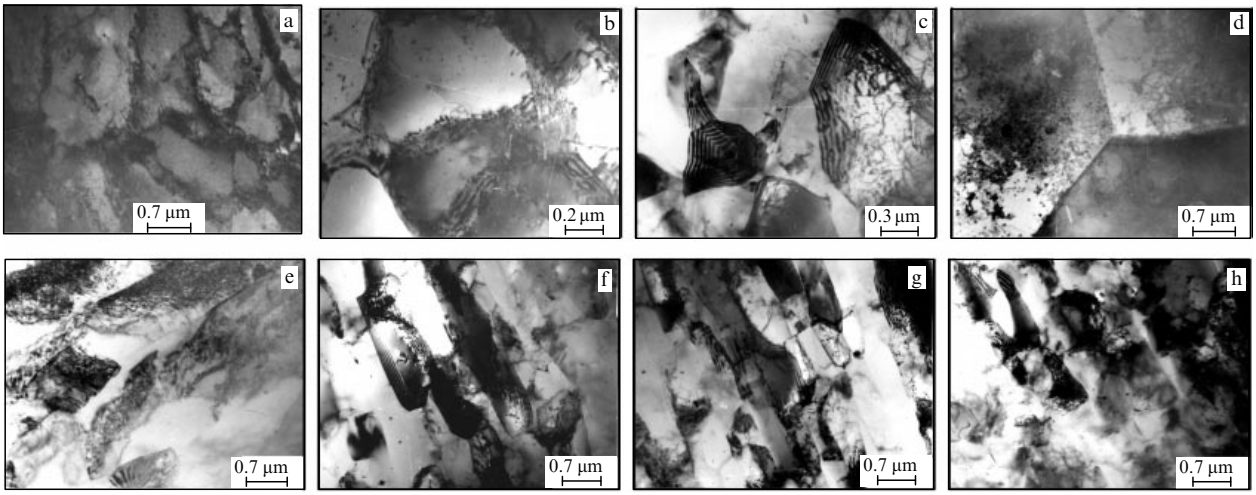

Figure 6. Changes in the BD1 alloy (Al–Cu–Mg) structure in the course of radiation annealing (a–h). (a–d) *Rolling-plane microstructure* of the BD1 *alloy*: (a) Initial post-cold-rolling state, cellular dislocation structure; (b) after-furnace annealing (250 °C, 2 h), uniform subgrain structure; (c) after-irradiation by Ar^+ ions ($E = 20$ keV, $j = 150$ μA cm^{-2}, $D = 10^{15}$ cm^{-2}, exposure time 1 s), subgrain structure; (c) the same with $D = 10^{17}$ cm^{-2}, recrystallized state. (e–h) *Cross-section microstructure* of a BD1 alloy sheet: (e) in the original state; (f–h) after irradiation by an Ar^+ ion beam with $D = 10^{16}$ cm^{-2} (near the irradiated surface, in the bulk, and near the nonirradited surface, respectively).

bombardment) offers an alternative to furnace annealing, an alternative that historically has never existed in the fields of production and treatment of metals and alloys. The phenomenon of radiation annealing is due to the RD effect of particle radiation, which is described in Sections 1–3.

Radiation annealing in aluminum [43–46, 51] and other alloys [27, 29, 31–33, 39–41] requires much lower temperatures (200 K less for aluminum alloys) and takes less time and much less energy than its thermal treatment.

Among entirely new findings, it is noteworthy that accelerated ion beams extend their influence very deep (3 mm or more for aluminum alloys) into a one-side-irradiated material; this is well confirmed by metallographic and electron microscope sheet cross section studies (Fig. 6).

In a cold-rolled state, the aluminum alloy systems studied, Al–Mg [43, 51], Al–Cu–Mg–Mn [45] and Al–Li–Cu–Mg–Zr [44], exhibit a well developed cellular dislocation structure, with dense dislocation entanglements as cell boundaries.

In the course of radiation annealing, the following processes were observed in the entire bulk of alloys (in the form of 3 mm thick sheets): polygonization with the formation of subgrains (for doses of $10^{15}-10^{16}$ cm^{-2}, the corresponding irradiation time is $\sim 1-10$ s), dissolution (10^{15} cm^{-2}) and formation ($10^{16}-10^{17}$ cm^{-2}) of new phases,[8] and the recrystallization and growth of grains ($5\times10^{16}-3\times10^{17}$ cm^{-2}) (see Fig. 6). In addition, as the radiation dose increases, the crystallographic *rolling texture* is steadily removed (Fig. 7) via a process similar to but distinct from furnace annealing [46]. The fast polygonization process involving the formation of grains is presumably due to the radiation-induced explosive rearrangement of the dislocation structure [44].

Using regression analysis techniques, the strength limit σ_B, the yield strength $\sigma_{0.2}$, and the unit elongation δ were obtained as (multidimensional) functions of the radiation parameters (the energy E, the ion current density j, and the dose D) (Fig. 5f).

[8] In furnace annealing, the intermetalilic composition of aluminum alloys remains unchanged.

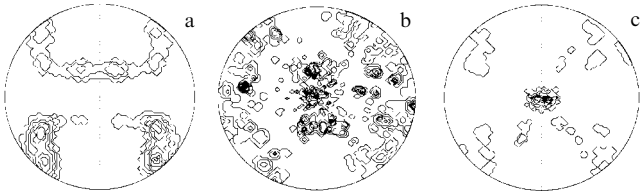

Figure 7. How the 1441 alloy (AL–Li–Cu–Mg) changes its crystallographic texture in the course of radiation annealing. (200) *pole figures*: (a) post-cold-rolling state, (b) after furnace annealing at 370 °C for 2 h, (c) after irradiation by Ar^+ ions ($D = 5.6\times10^{16}$ cm^{-2}).

To realize radiation annealing technology, special facilities and equipment have been developed (Fig. 8), including a service model of a *ribbon source* of ions with the beam cross section 20×1200 mm for the radiation annealing of sheet-rolled products [52] (Fig. 8c); a facility for the two-side treatment of moving sheets of aluminum alloys by counter beams of accelerated ions (with a special source for industrial applications [53]) (Fig. 8a, b); and a facility for the crystallization of alloys under irradiation (Fig. 8d).

5. Conclusion

To summarize, there is, in fact, no alternative to the radiation dynamic action as a way to initiate self-propagating structure–phase transformations in metastable media in order to modify their properties. Using a chemical explosion with the characteristic time $\tau = 10^{-5}$ s requires, in accordance with Eqn (2), increasing the zone of volume energy release ($d_0 = 2R_0$) to several centimeters and increasing the energy release rate to about that produced by a meteorite or a military propellant, which is clearly unacceptable given our purposes. Furthermore, other similarity aspects of influences under considerations should be given a detailed analysis.

Figure 8. Equipment for the radiation treatment of materials by ion beams. (a) Ion implanter for the bilateral treatment of moving alloy sheets by counter ion beams [52]. (b) Counter ion beams photographed through the chamber window. (c) Service model of a ribbon source of accelerated ions with the cross section 20 × 1200 mm for the treatment of sheet rolled products [53]. (d) Facility for the radiation treatment of melts.

Based on the above, the following conclusions can be drawn.

(1) Various particle radiations, except for the radiation of particles lighter than a nucleon, produce zones of explosive energy release in condensed media, emitting shock waves in the process. The energy density in such a zone can exceed 0.5 eV per atom. The energy carried away by the shock wave is sufficient to initiate a transition in metastable media into a state with a lower free energy.

(2) Even for a relatively small positive balance of the phase transition ($\Delta F' \sim (0.01-0.1)\Delta f$), the particle irradiation can initiate self-sustained (self-propagating) phase transformations at the fronts of post-cascade nanoshock waves. Such transformations explain the nature of the low-dose effect and of dynamic long-range effects observed under irradiation.

(3) Hydrodynamically described irradiation-induced shock wave processes and phase transformations, as well as structural chain-reaction-type rearrangements initiated by the propagation of waves (related to the unblocking of dislocations, annihilation of various types of defects [44], etc.), have been termed *radiation-dynamic* effects, as opposed to the well-studied radiation-stimulated migration processes.

(4) The plastic flow of material at the front of a post-cascade wave can be an alternative to diffusive mass transfer in condensed media. The mobility of atoms also increases with a decrease in the activation energy for atomic migration (all the way to making the process activationless) due to the lattice being radiationally 'shaken' by the emitted waves.

(5) Experimental data suggest that processes most affected by RD are those not requiring long-range mass transfer, such as massive (martensite) transformations, atomic disorder – order transformations, the aging of oversaturated solid solutions with the precipitation of disperse phases, and explosive dislocation rearrangements, etc.

(6) The concept of the radiation-dynamic effect of radiations on metastable media suggests the *radiation annealing* of condensed media as an alternative to furnace annealing. The efficiency of radiation annealing has been demonstrated by the improvement in the electric and magnetic properties of materials and by the increase in the plasticity of aluminum alloys (the removal of cold work). States that can be achieved with radiation annealing may differ widely from those occurring with furnace annealing, offering new possibilities for controlling the material properties. Radiation annealing

consumes much less energy, takes less time, and allows a reduction of 50 to 200 K in temperature.

References

1. Mamontov A P, Chernov I P *Effect Malykh Doz Ioniziruyushchego Izlucheniya* (Low Dose Effect of Ionizing Radiation) (Moscow: Energoatomizdat, 2001)
2. Tetel'baum D I, Kuril'chik E V, Latysheva N D *Neorg. Mater.* **35** 1 (1999) [*Inorganic Mater.* **35** 344 (1999)]
3. Guseva M I "Ionnaya implantatsiya v nepoluprvodnikovye materialy" ("Ion implantation and nonsemiconductor materials"), in *Itogi Nauki i Tekhniki* (Ser. Puchki Zaryazhennykh Chastits i Tverdoe Telo. Fizicheskie Osnovy Lazernoi i Puchkovoi Tekhnologii) (Advances in Science and Technology (Ser. Charged Particle Beams and Solid State. Physical Fundamentals of Laser and Beam Technology)) Vol. 5 (Moscow: VINITI, 1984) p. 5
4. Martynenko Yu V "Effekty dal'nodeistviya pri ionnoi implantatsii" ("Long-range effects at ion implantation"), in *Itogi Nauki i Tekhniki* (Ser. Puchki Zaryazhennykh Chastits i Tverdoe Telo) (Advances in Science and Technology (Ser. Charged Particle Beams and Solid State)) Vol. 7 (Moscow: VINITI, 1993) p. 82
5. Kirsanov V V, Suvorov A L, Trushin Yu V *Protsessy Radiatsionnogo Defektoobrazovaniya v Metallakh* (Radiation Defect Formation in Metals) (Moscow: Energoatomizdat, 1985)
6. Ibragimov Sh Sh, Kirsanov V V, Pyatiletov Yu S *Radiatsionnye Povrezhdeniya Metallov i Splavov* (Radiation Damage of Metals and Alloys) (Moscow: Energoatomizdat, 1985)
7. Wolfer W *Los Alamos Sci.* **26** 227 (2000)
8. Didenko A N et al. *Effekty Dal'nodeistviya v Ionno-Implantirovannykh Metallicheskikh Materialakh* (Long-Range Effects in Ion Implanted Metal Materials) (Exec. Ed. Yu P Kolobov) (Tomsk: Izd. NTL, 2004)
9. Ryssel H, Ruge I *Ionenimplantation* (Stuttgart: Teubner, 1978) [Translated into English: *Ion Implantation* (Chichester: Wiley, 1986); Translated into Russian (Moscow: Nauka, 1983)]
10. Thompson M W *Defects and Radiation Damage in Metals* (London: Cambridge Univ. Press, 1969) [Translated into Russian (Moscow: Mir, 1971)]
11. Biersack J P, Haggmark L G *Nucl. Instrum. Methods* **174** 257 (1980)
12. Poate J M, Foti G, Jacobson D C (Eds) *Surface Modification and Alloying by Laser, Ion, and Electron Beams* (New York: Plenum Press, 1983) [Translated into Russian (Moscow: Mashinostroenie, 1987)]
13. Chudinov V G, Cotterill R M J, Andreev V V *Phys. Status Solidi A* **122** 111 (1990)
14. Levin V M, Chernozatonskii L A, in *Fizicheskaya Entsiklopediya* (Encyclopedia of Physics) (Ed.-in-Chief A M Prokhorov) (Moscow: Sovetskaya Entsiklopediya, 1990) p. 507
15. Nordlung K et al. *Nature* **398** 49 (1999)
16. Kozlov A V et al. *Voprosy Atomnoi Nauki Tekh.* **66** (1) 47 (2006)
17. Amirkhanov I V et al. *Fiz. Elem. Chastits At. Yadra* **37** 1592 (2006) [*Phys. Part. Nucl.* **37** 837 (2006)]
18. Behrisch R et al. *Sputtering by Particle Bombardment* Vol. 3 *Characteristics of Sputtering Particles, Technical Applications* (Topics in Applied Physics, Vol. 64, Ed. R Behrisch) (Berlin: Springer-Verlag, 1991) [Translated into Russian (Moscow: Mir, 1998)]
19. Ovchinnikov V V et al., in *Trudy XV Mezhdunar. Soveshch.* "*Radiatsionnaya Fizika Tverdogo Tela*" (Proc. of the VII Intern. Symp. on Radiation Physics of Solids) (*Sevastopol', 4 – 9 July 2005*) (Ed. G G Bondarenko) (Moscow: NII PMT MGIEM (TU), 2005) p. 199
20. Didenko A N, Ligachev A E, Kurakin I B *Vozdeistvie Puchkov Zaryazhennykh Chastits na Poverkhnost' Metallov i Splavov* (Effect of Charged Particle Beams on Metal and Alloy Surfaces) (Moscow: Energoatomizdat, 1987)
21. Ovchinnikov V V et al. *Appl. Phys. A* **83** 83 (2006)
22. Zhukov V P, Boldin A A *At. Energ.* **63** 375 (1987) [*At. Energy* **63** 884 (1987)]
23. Zhukov V P, Ryabenko A V *Radiation Effects Defects Solids* **82** 85 (1984)
24. Zhukov V P, Demidov A V *At. Energ.* **59** (1) 29 (1985) [*At. Energy* **59** 568 (1985)]
25. Thompson D A *Radiation Effects Defects Solids* **56** 105 (1981)
26. Bleikher G A, Krivobokov V P, Pashchenko O V *Teplomassoperenos v Tverdom Tele pod Vozdeistviem Moshchnykh Puchkov Zaryazhennykh Chastits* (Thermal Mass Transfer in Solids under High-Power Charge Particle Beams) (Novosibirsk: Nauka, 1999)
27. Ovchinnikov V V, Chernoborodov V I, Ignatenko Yu G *Nucl. Instrum. Meth. Phys. Res. B* **103** 313 (1995)
28. Psakh'e S G et al. *Pis'ma Zh. Tekh. Fiz.* **25** (6) 7 (1999) [*Sov. Tech. Phys. Lett.* **25** 209 (1999)]
29. Ovchinnikov V V *Proc. SPIE* **2259** 605 (1994)
30. Ovchinnikov V V, Erkabaev M A, in *Trudy VII Mezhnats. Soveshch.* "*Radiatsionnaya Fizika Tverdogo Tela*" (Proc. of the VII Intern. Symp. on Radiation Physics of Solids) (*Sevastopol', 30 June – 5 July 1997*) (Ed. G G Bondarenko) (Moscow: NII PMT pri MGIEM (TU), 1997) p. 22
31. Borodin S N et al. *Pis'ma Zh. Tekh. Fiz.* **15** (17) 51 (1989)
32. Kreindel' Yu E, Ovchinnikov V V *Fiz. Khim. Obrabotki Mater.* (3) 14 (1991)
33. Kreindel Yu E, Ovchinnikov V V *Vacuum* **42** (1 – 2) 81 (1991)
34. Ovchinnikov V V et al. *Surf. Coating Technol.* **64** 1 (1994)
35. Ovchinnikov V V *Izv. Ross. Akad. Nauk Metally* (6) 104 (1996)
36. Mel'nikov L A, Sokolov B K, Stregulin A I *Fiz. Met. Metalloved.* **15** (3) 357 (1963)
37. Gushchina N et al., in *Trudy XII Mezhdunar. Konf.* "*Radiatsionnotermicheskie Effekty i Protsessy v Neorganicheskikh Materialakh*" (Proc. of the XII Intern. Conf. on Radiation Physics and Chemistry of Inorganic Materials) (Ed. A P Surzhikov) (Tomsk: Izd. Tomsk. Politekh. Univ., 2003) p. 192
38. Ovchinnikov V V et al., in *Trudy XIII Mezhdunar. Soveshch.* "*Radiatsionnaya Fizika Tverdogo Tela*" (Proc. of the XIII Intern. Symp. on Radiation Physics of Solids) (Ed. G G Bondarenko) (Moscow: NII PMT MGIEM (TU), 2003) p. 587
39. Chemerinskaya L S et al., in *Trudy XV Mezhdunar. Soveshch.* "*Radiatsionnaya Fizika Tverdogo Tela*" (Proc. of the XV Intern. Symp. on Radiation Physics of Solids) (*Sevastopol', 4 – 9 July 2005*) (Ed. G G Bondarenko) (Moscow: NII PMT MGIEM (TU), 2005) p. 461
40. Chemerinskaya L S et al., in *Trudy IV Mezhdunar. Nauch. Konf.* "*Radiatsionno-termicheskie Effekty i Protsessy v Neorganicheskikh Materialakh*" (Proc. of the IV Intern. Conf. on Radiation Physics and Chemistry of Inorganic Materials) (Ed. A P Surzhikov) (Tomsk: Izd. Tomsk. Politekh. Univ., 2004) p. 278
41. Goloborodsky B Yu, Ovchinnikov V V, Semenkin V A *Fusion Sci. Technol.* **39** 1217 (2001)
42. Borodin S N et al. *Pis'ma Zh. Tekh. Fiz.* **15** (13) 87 (1989)
43. Ovchinnikov V V et al. *Izv. Vyssh. Uchebn Zaved. Ser. Fiz.* (8, Suppl.) 350 (2006)
44. Ovchinnikov V V et al. *Izv. Vyssh. Uchebn. Zaved. Ser. Fiz.* (2) 73 (2007) [*Russ. Phys. J.* **50** 177 (2007)]
45. Ovchinnikov V V et al. *Fiz. Met. Metalloved.* **105** 404 (2008) [*Phys. Met. Metallogr.* **105** 375 (2008)]
46. Ovchinnikov V V et al., in *Trudy VII Mezhdunar. Konf.* "*Vzaimodeistvie Izluchenii s Tverdym Telom*" (Proc. of the VII Intern. Conf. "Interaction of Radiations with Solids"), *Minsk, Belarus', 26 – 28 September 2007*, p. 143
47. Sokolov B K et al. *Fiz. Met. Metalloved.* **89** (4) 32 (2000) [*Phys. Met. Metallogr.* **89** 348 (2000)]
48. Dragoshanskii Yu N, Gubernatorov V V, Sokolov B K, Ovchinnikov V V *Dokl. Ross. Akad. Nauk* **383** 761 (2002) [*Dokl. Phys.* **47** 302 (2002)]
49. Gubernatorov V V et al. *Dokl. Ross. Akad. Nauk* **410** 194 (2006) [*Dokl. Phys.* **51** 493 (2006)]
50. Gubernatorov V V et al. "Sposob termomagnitnoi obrabotki magnitomyagkikh materialov" ("Thermomagnetic treatment of magnetically soft materials"), Invention Patent No. 2321644 (03.08.2006)
51. Shkol'nikov A R et al. *Izv. Tomsk. Politekh. Univ.* **308** (7) 58 (2005)
52. Gavrilov N V et al. *J. Vac. Sci. Technol. A* **14** 1050 (1996)
53. Gavrilov N V, Emlin D R, Bureev O A *Izv. Vyssh. Uchebn. Zaved. Ser. Fiz.* (8, Suppl.) 92 (2006)

PACS numbers: 05.10.Ln, **64.60.–i**, **75.40.–s**
DOI: 10.1070/PU2008v051n09ABEH006611

Critical properties of frustrated spin systems on a stacked triangular lattice

A K Murtazaev

1. Introduction

One of the fundamental problems in statistical physics is the study of phase transitions and critical phenomena in frustrated spin systems. Despite the achievements in this area of research, the question of building a rigorous and consistent microscopic theory remains central to the modern condensed matter physics [1]. The modern theory of phase transitions and critical phenomena is based mainly on the ideas put forward in the hypothesis of scaling and universality and in the renormalization group theory [1–4]. Analysis of the results obtained from studies of frustrated systems and spin systems with quenched nonmagnetic disorder has shown that many of these results go far beyond the modern theory of phase transitions and critical phenomena [3, 5, 6].

Most of the traditional theoretic and experimental studies of frustrated systems encounter serious difficulties in attempts to calculate the critical parameters and to determine the features, nature, and mechanisms of critical behavior [7, 8]. Therefore, phase transitions and critical phenomena are currently studied by Monte Carlo methods [7–13]. Only lately did the study of the immediate vicinity of the critical point by Monte Carlo methods become possible. The achievements in this field are not only due to the sharp increase in computing power but also a result of new ideas and methods being developed. In particular, special algorithms, known as replica algorithms, for Monte Carlo calculations have been developed to study frustrated systems.

Currently, the magnetic, thermal, and critical properties of frustrated spin systems are being carefully studied [12, 13, 15–20], and the reason is that frustrated systems have remarkable magnetic properties and a rich variety of phases and phase transitions caused by strong degeneracy and a high susceptibility of such systems to various perturbing interactions [21, 22]. Moreover, it is still unclear whether frustrated spin systems belong to a new universality class of critical behavior and its dependence on various factors, such as the type and magnitude of the interlayer exchange coupling, the next-nearest-neighbor interaction, anisotropy, and external magnetic field.

In this report, we consider the results of a Monte Carlo investigation of the critical properties of the model of a 3D Heisenberg antiferromagnet on a triangular lattice.

The interest in this model stems from the fact that antiferromagnets on a triangular lattice constitute an example of frustrated systems. By studying this model, we may hope to resolve the question of whether frustrated systems belong to a new universality class of critical behavior, which is still open for discussion [6–13]. Furthermore, many important physical properties of frustrated systems strongly depend on the lattice geometry (on the degree of frustration). These features may narrow the possible universality classes of critical behavior, but there is still much to be done in this respect.

The question of the dependence of the critical properties of frustrated systems on the magnitude of the interlayer exchange coupling is especially interesting. The critical exponents, which are highly sensitive parameters, may serve as indicators of the spatial crossover from the 3D critical behavior to the 2D one (and back). The data that are currently at our disposal are not sufficient to uniquely determine how the critical behavior of frustrated systems depends on the interlayer exchange coupling parameter, and the problem has yet to be solved [8, 9, 12, 13].

In addition, the dependence of the critical properties of frustrated systems on the type and magnitude of the interlayer exchange coupling is not described in the available literature.

In this review, within a single method, and using a reliable scheme based on a special algorithm for the Monte Carlo methods (the replica algorithm), we attempt to determine the values of the critical parameters of models of frustrated 3D Heisenberg antiferromagnets on a triangular lattice with the highest possible accuracy.

2. The model and the method

The Hamiltonian of a 3D Heisenberg antiferromagnet on a triangular lattice can be written as [3]

$$\mathrm{H} = -J\sum_{\langle ij\rangle}\mathbf{S}_i\mathbf{S}_j - J'\sum_{\langle ij\rangle}\mathbf{S}_i\mathbf{S}_j\,, \qquad (1)$$

where $\mathbf{S}_i = (S_i^x, S_i^y, S_i^z)$ is a three-component unit vector, and J and J' are the exchange coupling constants. Summation is over the nearest neighbors. The lattice consists of 2D triangular layers packed along the orthogonal axis. The first term in the right-hand side of Eqn (1) accounts for the intralayer exchange coupling J and the second term accounts for the interlayer coupling J'.

We use three models, called D_1, D_2, and D_3, to establish the effect of the type and magnitude of the interlayer exchange coupling on the nature of the critical behavior:

model D_1: $J<0,\ J'>0,\ |J|=|J'|$;
model D_2: $J<0,\ J'<0,\ |J|=|J'|$;
model D_3: $J<0,\ J'>0,\ |J|\neq|J'|$.

Frustrated spin systems are complicated objects, even for studies by Monte Carlo methods. As is known, near a critical point, Monte Carlo methods encounter what is known as the critical-slowing-down problem; this problem is even more acute with frustrated systems [7]. Moreover, a characteristic feature of frustrated systems is the problem of multiple valleys of local energy minima. Ordinary Monte Carlo methods are usually ill suited for solving this problem. Hence, many new variants of these methods have recently been developed that focus on studies of frustrated systems. Among these, the replica algorithms have proved to be the most powerful and effective in the studies of critical phenomena in frustrated systems [14].

In our investigation, we used the highly effective replica algorithm [14] of the following type:

(i) Two replicas X and X' with different temperatures T and T' are modeled simultaneously.

(ii) After one hundred Monte Carlo steps per spin have been completed, the replicas exchange data in accordance with the Metropolis scheme with the probability

$$w(X\to X') = \begin{cases} 1\,, & \Delta\leqslant 0\,,\\ \exp(-\Delta)\,, & \Delta>0\,, \end{cases}$$

where $\Delta = (T - T')(U - U')$, with U and U' being the respective internal energies of the first and second replicas.

In the replica exchange algorithm, a random walk along the 'temperature interval' is implemented for each replica, with each random walk stimulating a random walk in the potential energy field. This facilitates the solution of the problem of the system 'sticking' in many states with local energy minima.

The calculations were carried out for systems with periodic boundary conditions and with linear dimensions $L \times L \times L = N$, where $L = 9-30$ for the D_1 and D_3 models and $L = 12-42$ for the D_2 model. For the D_3 model, the ratio of the interlayer to intralayer exchanges varied in the interval $R = |J'/J| = 0.01-1.0$. To take the system out of the state of thermodynamic equilibrium, a section of $\tau_0 = 4.0 \times 10^5$ Monte Carlo steps per spin, which is several times longer than the nonequilibrium section, was cut out. The thermodynamic quantities were averaged along a Markov chain $\tau = 25\tau_0$ long. To increase the accuracy, the data obtained from ten different initial configurations were averaged.

3. Simulation results

To monitor the temperature behavior of the heat capacity and susceptibility, we used the expressions [1, 23–25]

$$C = NK^2\left(\langle U^2\rangle - \langle U\rangle^2\right), \tag{2}$$

$$\chi = \begin{cases} NK\left(\langle m^2\rangle - \langle m\rangle^2\right), & T < T_{\mathrm{N}}, \\ NK\langle m^2\rangle, & T \geqslant T_{\mathrm{N}}, \end{cases} \tag{3}$$

$$\chi_{\mathrm{ch}} = \begin{cases} NK\left(\langle m_{\mathrm{ch}}^2\rangle - \langle m_{\mathrm{ch}}\rangle^2\right), & T < T_{\mathrm{ch}}, \\ NK\langle m_{\mathrm{ch}}^2\rangle, & T \geqslant T_{\mathrm{ch}}, \end{cases} \tag{4}$$

where $K = |J|/k_{\mathrm{B}}T$, N is the number of particles, m is the magnetic order parameter, m_{ch} is the chiral order parameter, and χ_{ch} is the chiral susceptibility.

The order parameter m of the system is given by [9]

$$m = \frac{3}{N}\sqrt{\frac{\langle M_{\mathrm{A}}^2 + M_{\mathrm{B}}^2 + M_{\mathrm{C}}^2\rangle}{3}}, \tag{5}$$

where M_{A}, M_{B}, and M_{C} are the magnetization of the sublattices A, B, and C.

The magnetization of a sublattice is given by [9]

$$\left\langle |\mathbf{M}_r| \right\rangle = \left\langle \sqrt{S_x^2 + S_y^2 + S_z^2} \right\rangle, \qquad r = \mathrm{A}, \mathrm{B}, \mathrm{C}. \tag{6}$$

To calculate the chiral order parameter m_{ch} of the system, we use the expressions [10, 11]

$$m_{\mathrm{ch}p} = \frac{2}{3\sqrt{3}}\sum_{\langle ij\rangle}^{p}[\mathbf{S}_i \times \mathbf{S}_j]_z, \tag{7}$$

$$m_{\mathrm{ch}} = \frac{1}{N}\sum_{p} m_{\mathrm{ch}p}, \tag{8}$$

where the subscript p labels the triangular plaquettes.

Figures 1 and 2 show the temperature dependence of the heat capacity C and the susceptibility χ for models D_1 and D_2. Here and in what follows, the errors in the data do not exceed the size of the symbols in the figures. We note the distinct maxima in the critical region for both models, with the maxima occurring at the same temperature (within error).

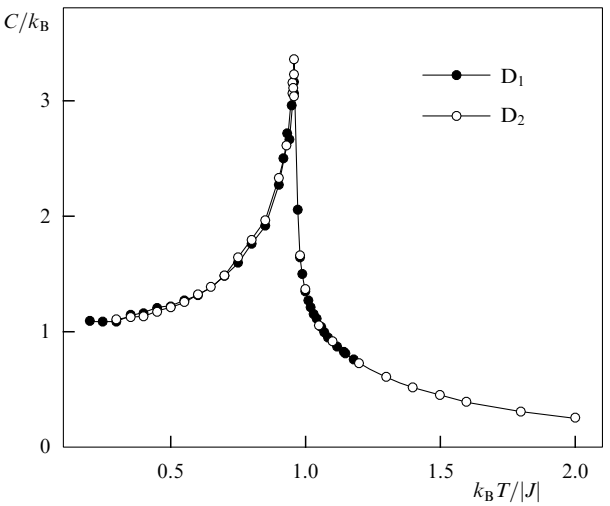

Figure 1. The heat capacity C/k_{B} as a function of the temperature $k_{\mathrm{B}}T/|J|$ for models D_1 and D_2.

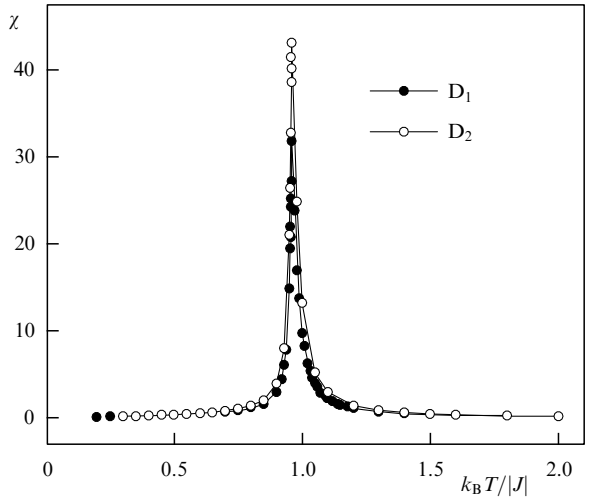

Figure 2. The susceptibility χ as a function of the temperature $k_{\mathrm{B}}T/|J|$ for models D_1 and D_2.

To determine the critical temperature T_{N} more accurately, we use the method of fourth-order Binder cumulants U_L, which are [26]

$$U_L = 1 - \frac{\langle m^4\rangle_L}{3\langle m^2\rangle_L^2}. \tag{9}$$

According to the finite-size scaling theory, the critical point is the point where all the temperature curves $U_L(T)$ intersect [25].

Figure 3 depicts the characteristic temperature dependence of U_L for model D_2. The inset shows the accuracy with which the critical temperature was determined. Clearly, the critical temperature at $R = 1$ is $T_{\mathrm{N}} = 0.957(1)$ (here and in what follows, the temperature is given in units of $|J|/k_{\mathrm{B}}$). In determining the chiral critical temperature T_{ch}, we used the cumulant crossing method, which is considered more accurate and reliable [11–13, 26, 27]. Similar calculations were done for models D_1 and D_3.

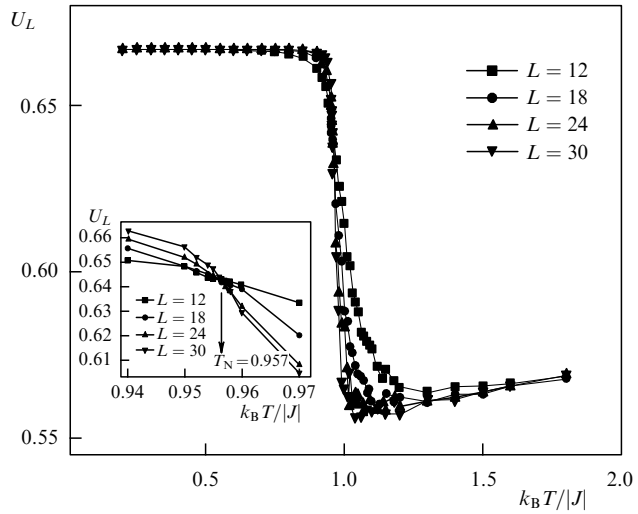

Figure 3. The Binder cumulant U_L as a function of the temperature $k_BT/|J|$ for model D_2.

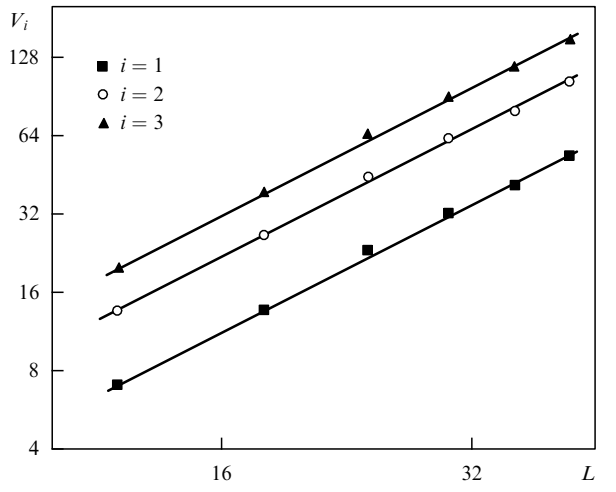

Figure 4. Dependence of the parameter V_i on the linear size L at $T = T_N$ for model D_2.

To calculate the static chiral and magnetic critical exponents of the heat capacity (α), of the susceptibilities (γ and γ_{ch}), of the magnetizations (β and β_{ch}), and of the correlation radii (ν and ν_{ch}), we used formulas from the finite-size scaling theory [24, 26–29].

It follows from the KPC relations that the following relations hold in a system with the dimensions $L \times L \times L$ at $T = T_N$ for sufficiently large L [11, 24, 28–31]:

$$m \propto L^{-\beta/\nu}, \tag{10}$$

$$m_{ch} \propto L^{-\beta_{ch}/\nu_{ch}}, \tag{11}$$

$$\chi \propto L^{\gamma/\nu}, \tag{12}$$

$$\chi_{ch} \propto L^{\gamma_{ch}/\nu_{ch}}, \tag{13}$$

$$V_n = L^{1/\nu} g_{V_n}, \tag{14}$$

$$V_{chn} = L^{1/\nu_{ch}} g_{V_n}, \tag{15}$$

where g_{V_n} is a constant and V_n and V_{chn} can be taken as

$$V_i = \frac{\langle m^i E\rangle}{\langle m^i\rangle} - \langle E\rangle, \qquad i = 1,2,3,4, \tag{16}$$

$$V_{chi} = \frac{\langle m_{ch}^i E\rangle}{\langle m_{ch}^i\rangle} - \langle E\rangle, \qquad i = 1,2,3,4. \tag{17}$$

These relations were used to determine β, β_{ch}, γ, γ_{ch}, ν, and ν_{ch}. In approximating the temperature dependence of the heat capacity on L, we used the expression [9–11, 32]

$$C_{max}(L) = A_1 - A_2 L^{\alpha/\nu}, \tag{18}$$

where A_1 and A_2 are some coefficients.

Figure 4 shows the characteristic curves representing the dependence of the parameters V_i for $i = 1, 2, 3$ on the lattice size L for model D_2 in the log-log scale. Clearly, points in the diagrams land on straight lines (within error). The diagrams in Fig. 4 obtained by the method of least squares are parallel straight lines, and their slopes determine the value of $1/\nu$. The value of ν calculated in this manner was used to determine the critical exponents of the heat capacity (α), susceptibility (γ), and magnetization (β). The chiral critical exponents were also determined through this scheme. Similar calculations were carried out for models D_1 and D_3.

All the values of the exponents thus obtained are listed in Table 1. The data in Refs [6, 7, 9–11] are also listed for comparison.

Of special interest is the procedure that was used to determine the Fisher exponent η. Starting from the relation between the susceptibility χ and the correlation radius ξ [33],

$$\chi \propto \xi^{\gamma/\nu}, \tag{19}$$

and using the relation $\eta = 2 - \gamma/\nu$ between the exponents η and ν, we obtain

$$\ln \frac{\chi}{\xi^2} = c - \eta \ln \xi, \tag{20}$$

where c is a constant. For a finite-size system at $T = T_N$, we have $\xi = L$. This yields

$$\ln \frac{\chi}{L^2} = c - \eta \ln L. \tag{21}$$

Using this formula, we determined the Fisher exponent η. The same approach was used to determine the magnetic and chiral critical Fisher exponents for models D_1 and D_2, which are also listed in Table 1.

The values of the magnetic and chiral critical temperatures for models D_1 and D_2 coincide, to within error, with each other and with those obtained in [9–11]. A comparison of the values of the critical exponents for model D_1 and the results for a similar model in [9, 11] shows that our data are close to those in the more recent paper [11]. Some of the critical parameters for model D_2 coincide, to within error, with the results for the same model in Ref. [10]. Table 1 shows that our data for model D_1 are closer to the experimental results (see the references in [6]) for the antiferromagnet $CsMnBr_3$ with a triangular lattice than to the data for model D_2. We note that this is the first time that the values of the Fisher exponents η and η_{ch} for models D_1 and D_2 have been calculated.

Table 1 clearly shows that our results are in good agreement with the data from laboratory experiments and

Table 1. Values of the critical parameters for a 3D Heisenberg antiferromagnet on a stacked triangular lattice.

Critical parameter	Our data		Monte Carlo method			Experiment (see references in [6])	Pure model (see references in [7])
	D_1	D_2	[9]	[10]	[11]		
T_N	0.956(1)	0.957(1)	0.954(2)	0.955(2)	0.9577(2)	—	1.443
T_{ch}	0.956(2)	0.957(2)	—	0.958(2)	0.9577(2)	—	—
ν	0.59(1)	0.64(1)	0.53(3)	0.59(2)	0.586(8)	0.57(3)	0.706(9)
α	0.26(2)	0.05(2)	0.4(1)	0.24(8)	—	0.40(5)	−0.117(2)
β	0.26(1)	0.30(1)	0.25(2)	0.30(2)	0.285(11)	0.25(1)	0.364(7)
γ	1.23(2)	1.36(2)	1.1(1)	1.17(7)	1.185(3)	1.10(5)	1.390(23)
ν_{ch}	0.59(2)	0.64(2)	—	0.60(2)	0.60(2)	—	—
β_{ch}	0.43(2)	0.52(2)	—	0.55(2)	0.50(2)	0.44(2)	—
γ_{ch}	0.87(3)	0.93(3)	—	0.72(2)	0.82(2)	0.84(7)	—
η	−0.09(3)	−0.06(3)	—	—	—	—	0.031(7)
η_{ch}	0.50(4)	0.63(4)	—	—	—	—	—

Table 2. Values of the magnetic critical parameters for model D_3.

R	T_N	ν	α	β	γ	$\alpha+2\beta+\gamma=2$
1	0.956(1)	0.59(2)	0.26(3)	0.26(2)	1.23(4)	2.02
0.8	0.872	0.60	0.24	0.26	1.26	2.02
0.7	0.829	0.61	0.22	0.28	1.29	2.07
0.6	0.783	0.59	0.22	0.29	1.22	2.02
0.4	0.677	0.60	0.24	0.27	1.27	2.05
0.3	0.619	0.60	0.26	0.29	1.23	2.07
0.1	0.468	0.59	0.24	0.28	1.17	1.97
0.075	0.442	0.55	0.26	0.24	1.23	1.97
0.05	0.413	0.55	0.15	0.22	1.11	1.70
0.01	0.353	0.48	0.09	0.27	0.82	1.45

Table 3. Values of the chiral critical parameters for model D_3.

R	T_{ch}	ν_{ch}	α	β_{ch}	γ_{ch}	$\alpha+2\beta_{ch}+\gamma_{ch}=2$
1	0.956(2)	0.59(2)	0.26(3)	0.43(2)	0.87(5)	1.99
0.8	0.872	0.60	0.24	0.42	0.96	2.04
0.7	0.829	0.61	0.22	0.48	0.96	2.14
0.6	0.783	0.59	0.22	0.46	0.85	1.99
0.4	0.677	0.60	0.24	0.43	0.90	2
0.3	0.619	0.60	0.26	0.48	0.81	2.03
0.1	0.468	0.59	0.24	0.47	0.82	2
0.075	0.442	0.55	0.26	0.42	0.87	1.97
0.05	0.413	0.55	0.15	0.31	0.60	1.37
0.01	0.353	0.48	0.09	0.40	0.52	1.41

with most results of numerical experiments by other researchers, but differ from the results for a nonfrustrated 3D Heisenberg antiferromagnet (see the references in [7]). This suggests that the 3D Heisenberg frustrated antiferromagnet on a stacked triangular lattice (model D_1) constitutes a new universality class of critical behavior.

Moreover, most of the critical exponents of model D_1 differ significantly from the critical exponents of model D_2. This suggests that the type of interlayer exchange coupling plays an important role in the formation of universality classes of such systems. It is obvious that models D_1 and D_2 belong to different universality classes and each has its own set of critical exponents.

The question of the dependence of the critical exponents on R is also of considerable interest. Furthermore, for the majority of real materials, the values of J and J' do not coincide [15–17, 20]. This question was studied for different values of R. Using a relation from the finite-size scaling theory and the above procedure, we were able to calculate all the main static chiral and magnetic critical exponents for $J<0$ and $J'>0$ with R ranging from 0.01 to 1.0. The values of the exponents obtained in this way are listed in Tables 2 and 3.

The data in Tables 2 and 3 show that for the values $R \geqslant 0.075$, the exponents coincide (within error) and scaling relations between the critical exponents hold with high accuracy. When $R \leqslant 0.05$, the critical exponents vary substantially and scaling relations are no longer valid. Apparently, $R = 0.075$ is the limit beyond which a crossover from the 3D critical behavior to the 2D critical behavior occurs.

4. Conclusion

The study of the critical properties of the 3D Heisenberg frustrated antiferromagnet on a stacked triangular lattice, whose results are presented in this report, has been done using the highly effective Monte Carlo replica algorithm. We have calculated the main static chiral and magnetic critical exponents. The critical exponents of heat capacity (α), susceptibilities (γ and γ_{ch}), order parameters (β and β_{ch}), Fisher exponents η and η_{ch}, and correlation radii (ν and ν_{ch}) were calculated using relations from the finite-size scaling theory within a single method and a single investigation. The values of the Fisher exponents η and η_{ch} for this model were calculated for the first time. Our results suggest that the 3D frustrated Heisenberg model antiferromagnet on a stacked triangular lattice belongs to a new universality class. The results of our investigation imply that the universality class of the critical behavior of the Heisenberg antiferromagnet on a triangular lattice depends on the type and magnitude of the interlayer exchange coupling.

This work was supported by the Russian Foundation for Basic Research (grant 07-02-00194 and the South Russia grant 06–02-96602) and the Russian Science Support Foundation.

References

1. Patashinskii A Z, Pokrovskii V L *Fluktuatsionnaya Teoriya Fazovykh Perekhodov* (Fluctuation Theory of Phase Transitions) 2nd ed. (Moscow: Nauka, 1982) [Translated into English (Oxford: Pergamon Press, 1979)]

2. Ma Sh *Modern Theory of Critical Phenomena* (Reading, Mass.: W.A. Benjamin, 1976) [Translated into Russian (Moscow: Mir, 1980)]
3. Dotsenko Vik S *Usp. Fiz. Nauk* **165** 481 (1995) [*Phys. Usp.* **38** 457 (1995)]
4. Korshunov S E *Usp. Fiz. Nauk* **176** 233 (2006) [*Phys. Usp.* **49** 225 (2006)]
5. Murtazaev A K *Usp. Fiz. Nauk* **176** 1119 (2006) [*Phys. Usp.* **49** 1092 (2006)]
6. Maleev S V *Usp. Fiz. Nauk* **172** 617 (2002) [*Phys. Usp.* **45** 569 (2002)]
7. Kamilov I K, Murtazaev A K, Aliev Kh K *Usp. Fiz. Nauk* **169** 773 (1999) [*Phys. Usp.* **42** 689 (1999)]
8. Loison D et al. *Pis'ma Zh. Eksp. Teor. Fiz.* **72** 487 (2000) [*JETP Lett.* **72** 337 (2000)]
9. Kawamura H *J. Phys. Soc. Jpn.* **56** 474 (1987)
10. Kawamura H *J. Phys. Soc. Jpn.* **61** 1299 (1992)
11. Mailhot A, Plumer M L, Caille A *Phys. Rev. B* **50** 6854 (1994)
12. Murtazaev A K, Ramazanov M K, Badiev M K *Zh. Eksp. Teor. Fiz.* **132** 1152 (2007) [*JETP* **105** 1011 (2007)]
13. Murtazaev A K, Ramazanov M K *Phys. Rev. B* **76** 174421 (2007)
14. Mitsutake A, Sugita Y, Okamoto Y *Biopolymers* **60** 96 (2001)
15. Svistov L E et al. *Phys. Rev. B* **67** 094434 (2003)
16. Svistov L E et al. *Pis'ma Zh. Eksp. Teor. Fiz.* **80** 231 (2004) [*JETP Lett.* **80** 204 (2004)]
17. Svistov L E et al. *Pis'ma Zh. Eksp. Teor. Fiz.* **81** 133 (2005) [*JETP Lett.* **81** 102 (2005)]
18. Pelissetto A, Rossi P, Vicari E *Phys. Rev. B* **65** 020403 (2001)
19. Peles A, Southern B W *Phys. Rev. B* **67** 184407 (2003)
20. Smirnov A I et al. *Phys. Rev. B* **75** 134412 (2007)
21. Gekht R S *Zh. Eksp. Teor. Fiz.* **102** 1968 (1992) [*JETP* **75** 1058 (1992)]
22. Gekht R S *Usp. Fiz. Nauk* **159** 2 (1989) [*Sov. Phys. Usp.* **32** 871 (1989)]
23. Binder K, Wang J-Sh *J. Stat. Phys.* **55** 87 (1989)
24. Peczak P, Ferrenberg A M, Landau D P *Phys. Rev. B* **43** 6087 (1991)
25. Binder K, Heermann D W *Monte Carlo Simulation in Statistical Physics* (Berlih: Springer-Verlag, 1988) [Translated into Russian (Moscow: Nauka, 1995)]
26. Binder K *Z. Phys. B* **43** 119 (1981)
27. Ferrenberg A M, Landau D P *Phys. Rev. B* **44** 5081 (1991)
28. Ferdinand A E, Fisher M E *Phys. Rev.* **185** 832 (1969)
29. Fisher M E, Barber M N *Phys. Rev. Lett.* **28** 1516 (1972)
30. Landau D P *Physica A* **205** 41 (1994)
31. Loison D *Phys. Lett. A* **257** 83 (1999)
32. Murtazaev A K, Kamilov I K, Magomedov M A *Zh. Eksp. Teor. Fiz.* **120** 1535 (2001) [*JETP* **93** 1330 (2001)]
33. Holm Ch, Janke W *Phys. Rev. B* **48** 936 (1993)

PACS numbers: **42.55.–f**, 42.60.By, **42.65.–k**
DOI: 10.1070/PU2008v051n09ABEH006612

Petawatt lasers based on optical parametric amplifiers: their state and prospects

E A Khazanov, A M Sergeev

1. Introduction

A review of current state-of-the-art femtosecond lasers with the currently record power of the order of 1 PW is presented. Based on an analysis of the advantages and drawbacks of parametric amplification in comparison with laser amplification in a neodymium glass and sapphire crystal, it is shown that the use of parametric amplifiers is a promising approach to overcoming a petawatt barrier. Other concepts concerning multipetawatt lasers, including those based on the unique properties of laser ceramics, are also discussed.

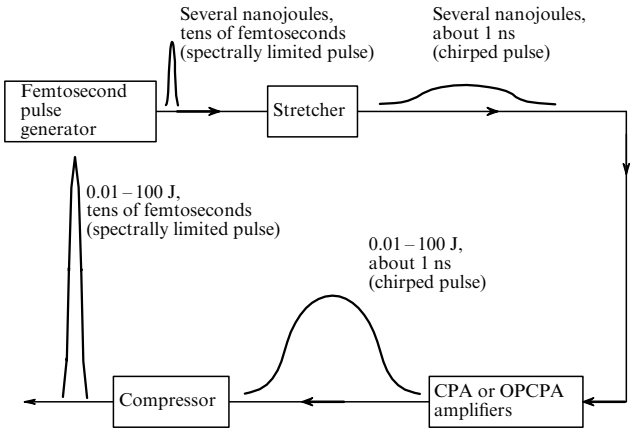

Figure 1. General drawing of powerful femtosecond lasers.

Since the creation of the first laser, one of the main goals of quantum electronics has been an increase in the peak power of laser radiation. The term 'high peak power' is continuously changing, and we are currently speaking of a power about 1 PW (10^{15} W). The key milestone that allowed obtaining such a power was the invention [1] of a fundamental principle, the amplification of chirped (stretched in time, frequency-modulated) pulses, CPA (chirped pulse amplification). The idea (see Fig. 1) is that prior to amplification, a femtosecond pulse is stretched to a duration of approximately 1 ns, which reduces its power and allows amplifying it to high energy without self-focusing and breakdown. Then the pulse is compressed to the initial duration using diffraction gratings with a high breakdown threshold, because light is only reflected from the gratings, not passing inside a material medium. The CPA principle is used without exception in all lasers with the power 1 TW or greater.

Petawatt power was first obtained in 1996 on the basis of CPA in neodymium glass [2]; the pulse duration was 440 fs and the energy was 600 J. The invention of sapphire crystal (corundum with titanium) [3] allowed obtaining considerably shorter pulses and resulted in the creation of a petawatt laser [4] with the much lower pulse energy of 28 J at the duration 33 fs. In Ref. [5], it was suggested to use the parametric amplification (optical parametric chirped pulse amplification, OPCPA) instead of the conventional laser amplification. The first petawatt OPCPA laser was created [6] in 2006 on the basis of a nonlinear DKDP crystal (Deuterated Potassium Dihydrogen Phosphate).

Thus, all existing petawatt lasers and those under development can be divided into three groups by the amplifying medium: (1) neodymium glass [2, 7–14], (2) sapphire (corundum with titanium) [4, 13, 15–17], and (3) parametric amplifiers on KDP (Potassium Dihydrogen Phosphate) and DKDP crystals [6, 18–25] (see Table 1). In all the groups, energy (in the form of population inversion) is stored in neodymium ions in a glass. In the first case, this energy is directly converted to the energy of a chirped pulse, which is then compressed. In the second and third cases, the stored energy is converted into the energy of a narrow-band nanosecond pulse, which is converted into a second harmonic and serves to pump the chirped pulse amplifiers. This pumping either provides the population inversion in a sapphire crystal or decays parametrically into two chirped pulses in a nonlinear crystal.

Table 1. Comparison of petawatt lasers concepts. Symbols '+', '−', and '0' indicate characteristics that are above average, below average, and average, respectively.

Amplifying medium	Nd:glass		Ti:sapphire		DKDP		Cr:YAG-ceramics	
Energy source	Nd:glass		Nd:glass		Nd:glass		Nd:glass	
Pumping	no	(+)	2ω Nd*	(−)	2ω Nd	(−)	1ω Nd**	(0)
Pumping duration, ns	no	(+)	> 10	(0)	1	(−)	> 10	(0)
Amplifier aperture, cm	40	(0)	8	(−)	40	(0)	> 50	(+)
Minimal duration, fs	250	(−)	25	(+)	25	(+)	25	(+)
Efficiency (1ω Nd → fs)***, %	80	(+)	15	(0)	10	(−)	25	(0)
Number of petawatts from 1 kJ 1ω Nd	3.2 (3)****		6 (1.5)****		4		10	
Power obtained, PW	1.36 [2]		0.85 [4]		0.56 [23]		—	

* Second harmonic of a neodymium laser.
** First harmonic of a neodymium laser.
*** From the first-harmonic pulse of a neodymium laser to a femtosecond pulse.
**** Resistance of diffraction gratings and sapphire crystals limit the maximum power at the respective levels of 3 PW and 1.5 PW.

The peak power is determined by the duration and energy of a compressed pulse. The maximal energy is obtained in neodymium glass lasers because the energy stored in the form of population inversion is directly converted into a chirped pulse. However, a narrow-band gain of neodymium glass limits the duration of the compressed pulse to several hundred femtoseconds. As a result, the optical resistance of diffraction gratings hinders extension into the multipetawatt range.

In contrast to neodymium glass lasers, sapphire lasers provide wide-band gain, which allows compressing a pulse down to 10–20 fs. But the aperture of sapphire crystals is below 10 cm. In attempting to surpass the petawatt level, so small an aperture would limit the energy of a chirped pulse due to optical breakdown and self-focusing.

2. Advantages and drawbacks of parametric amplification

Parametric amplifiers have none of the drawbacks of sapphire and neodymium glass mentioned above because the aperture of modern nonlinear KDP and DKDP crystals is 40 cm, which is comparable to the dimensions of neodymium glass elements, and the gain width is close to that of sapphire. Moreover, the OPCPA approach has unquestionable advantages compared to CPA.

First, OPCPA provides a very high single-pass gain, up to 10^4, compared to 10 for CPA. Second, in the case of OPCPA, the amplification is directed, which eliminates enhanced spontaneous luminescence and self-oscillation of amplifiers in transverse directions, removing the substantial limitation of CPA lasers. Third, the low level of amplified spontaneous luminescence in the longitudinal direction provides a high temporal contrast of the compressed pulse. Fourth, in the case of OPCPA, in contrast to CPA, the energy difference between the pump and the signal quanta is not released in the crystal in the form of heat because it is withdrawn by an idle wave. This provides low thermal load and, as a consequence, diffraction beam quality even in the pulse-repetition mode. Finally, the spectrum of a chirped pulse is less distorted by gain saturation in the case of OPCPA than for CPA because the effect of the population inversion reduction at the end of the pulse is absent. Hence, the use of parametric amplifiers is rather promising for overcoming the petawatt barrier.

Nevertheless, OPCPA has drawbacks. First of all, there is the requirement of a short (about 1 ns) duration of the pumping pulse, because a parametric amplifier, in contrast to a laser amplifier, cannot acquire energy due to population inversion. Due to the same reason, a high accuracy (of the order of 100 ps) is needed in synchronizing the pumping and chirped pulses. In addition, in the case of OPCPA, it is actually impossible to use several lasers for pumping a single amplifier, which is easily realized in the case of CPA.

It follows that all the advantages of OPCPA are directly related to the amplifier, whereas its drawbacks are related to the pumping laser, where the requirements are higher than for CPA.

3. Choosing the nonlinear crystal for OPCPA

The most promising pumping for powerful parametric amplifiers is the second-harmonic radiation of neodymium glass lasers with the wavelength $\lambda_p = 527$ nm. At this wavelength, the widest gain band is observed for LBO (lithium borate), BBO (barium metaborate), KDP, and DKDP crystals [26, 27]. The first two types of crystals have large nonlinearity; but the modern growing technology is capable of producing such crystals with the transverse dimension of at most several centimeters. Hence, LBO and BBO crystals can only be used in the first cascades of OPCPA. KDP and DKDP crystals with lower nonlinearity can be produced with the dimension that provides the aperture of 40 cm and more, which allows using them in final stages of petawatt OPCPA lasers.

Of key importance for wide-band parametric amplification are the dispersion dependences of the refractive index, which determine the wave-vector mismatch Δk. The mismatch be presented in the form of a Taylor series with respect to the deviation Ω from the central frequency of three-wave synchronism,

$$\Delta k(\Omega) \equiv \Delta k(0) - \left(\frac{\mathrm{d}k_s}{\mathrm{d}\omega} + \frac{\mathrm{d}k_{iz}}{\mathrm{d}\omega}\right)\Omega - \frac{1}{2}\left(\frac{\mathrm{d}^2k_s}{\mathrm{d}\omega^2} + \frac{\mathrm{d}^2k_{iz}}{\mathrm{d}\omega^2}\right)\Omega^2 - O(\Omega^3),$$

where k_s is the wave vector of the signal wave propagating along the z axis and k_{iz} is the projection of the idle-wave

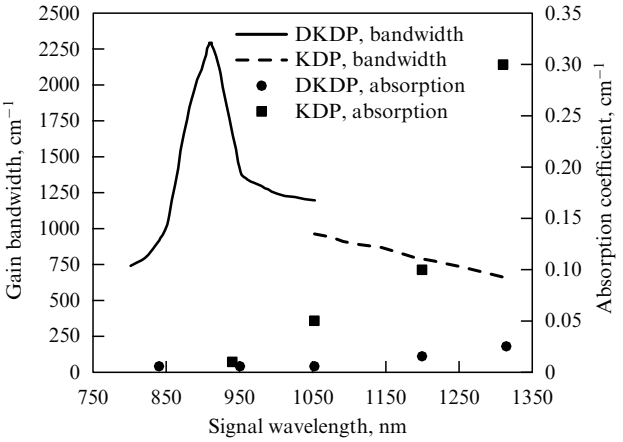

Figure 2. Absorption coefficient for the ordinary wave and the gain bandwidth full width at half maximum at the pumping intensity 1 GW cm^{-2}, wavelength $\lambda_p = 527$ nm, and crystal length 70 mm [27].

vector onto the z axis. Depending on the number of zero terms in the series, we are dealing with phase matching (only the first term is zero), group phase matching (the first two terms are zero), or ultra-wide phase matching (the first three terms are zero). The last case requires the fulfillment of three conditions. At a prescribed wavelength of the pumping radiation λ_p, there are three free parameters: two angles (between the optical axis of the crystal and the wave vectors of pumping and signal radiation) and the signal wavelength λ_s. The analysis in [27] shows that for crystals with $\lambda^* > 2\lambda_p$, there exists a set of three parameters such that the three conditions for ultra-wide synchronism are fulfilled, and for crystals with $\lambda^* < 2\lambda_p$, these three conditions never hold and ultra-wide phase matching is absent. Here, λ^* is the wavelength at which the second derivative of the wavenumber for an ordinary wave vanishes: $d^2k/d\omega^2 = 0$.

At $\lambda^* < 2\lambda_p$, the maximum bandwidth of gain is achieved when the interaction degenerates ($\lambda_s = 2\lambda_p$). To such crystals, we can assign KDP, which was considered the only candidate for high-power OPCPA lasers in [18, 19, 26, 28–31]. Nevertheless, as can be seen in Fig. 2, the maximum band of gain in KDP does not exceed 1000 cm^{-1} and occurs at $\lambda_s = 2\lambda_p = 1054$ nm, i.e., in a range where no lasers exist with the duration 30 fs or less.

In Ref. [32], it was suggested to use DKDP crystals instead of KDP. In Refs [27, 32, 33], reliable dispersion functions were determined for DKDP and the influence of the degree of deuteration was considered. It was also shown that for DKDP, we have $\lambda^* < 2\lambda_p$ and the conditions of ultrawide phase matching hold at $\lambda_s = 910$ nm. In this case, the gain band is twice as wide as that in KDP (see Fig. 2), which allows amplifying pulses with the duration ~ 15 fs. It is important that at both the signal (910 nm) and idler (1250 nm) wavelengths, there are sources of femtosecond pulses with this duration, namely sapphire and cromium–forsterite lasers [34, 35]. In addition, DKDP crystals have a noticeably lower absorption (see Fig. 2).

Thus, the most promising architecture of petawatt OPCPA lasers is the amplification of a chirped pulse with the central wavelength 910 nm in a DKDP crystal. In Section 4, an OPCPA laser with this architecture and the power 0.56 PW is considered [23].

4. 0.56-petawatt OPCPA laser on a DKDP crystal

The general schematic of the laser created at the Institute of Applied Physics (IAP) of the RAS is shown in Fig. 3. As was mentioned in Section 3, a signal wave (sapphire laser, $\lambda_s = 910$ nm) or idler wave (cromium–forsterite laser, $\lambda_s = 1250$ nm) can be injected into a DKDP crystal. The second variant was used in [23], where the master oscillator was a cromium–forsterite laser emitting pulses with the duration 40 fs and energy 3 nJ. Before amplification, the pulses were extended in a stretcher.

Stretching a pulse at one wavelength (idle) and compressing it at another (signal) wavelength requires a nonstandard dispersion characteristic of the stretcher. Calculations show

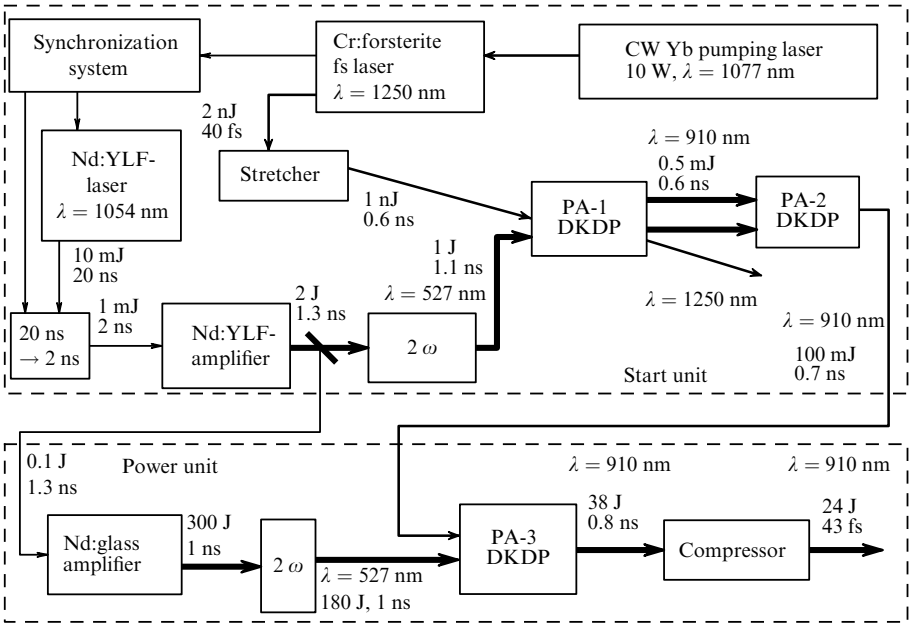

Figure 3. Drawing of an OPCPA laser with the power 0.56 PW [23]. (PA is the parametrical amplifier).

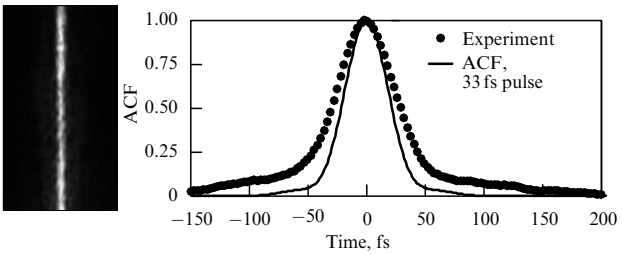

Figure 4. Autocorrelation function for the output pulse (photo and points) and for a Fourier-limited pulse with the duration 33 fs (solid curve) [23].

that such a characteristic is provided by a compressor with two prisms having similar vertex angles [36, 37]. Such a nonstandard stretcher based on a holographic diffraction grating (1200 mm^{-1}) extended a 40 fs pulse to the duration 0.6 ns with the transmission band 1000 cm^{-1}.

Two parametric amplifiers were first pumped by a single-mode Nd:YLF-laser with the energy of the second harmonic ($\lambda_p = 527$ nm) up to 1 J [38], synchronized with a Cr:forsterite laser to an accuracy of 50 ps [39]. The third parametric amplifier was pumped by the second harmonic of a neodymium glass laser with the energy 180 J and pulse duration 1 ns. Such high parameters were obtained due to the following key features of the pumping laser: high-efficiency amplifiers [40]; specific construction of spatial filters [41]; a system for radiation input to the amplifier, which provided the fill factor 0.8 for the output cascade; the use of circular polarization for two output amplifiers in order to suppress small-scale self-focusing [43]; and a frequency doubler with the first-type interaction, which provided a 70% conversion efficiency at the thermo-induced depolarization above 2% [44].

The first parametric amplifier was a two-pass one. On the first pass, it converts pulses with the wavelength 1250 nm into those of 910 nm, and on the second pass, it amplifies radiation at the wavelength 910 nm. The second amplifier was single-pass and had an efficiency $\sim 15\%$, which corresponds to numerical simulation results. The width of the spectrum of the amplified pulse was approximately 30% less than that of the injected signal. Upon further compression, pulses with the duration ~ 80 fs were obtained at the power 0.44 TW [20].

Due to saturation of the third parametric amplifier (with the DKDP crystal length 80 mm and the aperture 120 mm), the spectrum of a chirped pulse broadened, the energy of the pulse reached 38 J, and the amplifier efficiency was above 20%. Two diffraction gratings (1200 mm^{-1}) with the dimensions 24×35 cm were used in a compressor. The maximum energy of compressed pulses was 24 J. The autocorrelation function (see Fig. 4) corresponds to a 43 fs pulse duration full width at half maximum; thus, the peak power was 0.56 PW, which is 35 times greater than the power obtained earlier [19] in OPCPA lasers (see Fig. 5).

Due to the use of OPCPA and a compact pumping neodymium glass laser, the petawatt laser with all infrastructure elements resides in a laboratory with the area less than 80 m^2.

5. Prospects for expanding to the multipetawatt range

As mentioned in Section 4, one of the advantages of OPCPA lasers on DKDP crystals is the simplicity of scaling, which is now limited only by the pumping pulse energy. Four large projects are presently being implemented, which are aimed at obtaining multi-petawatt power for OPCPA lasers.

First of all, there is the Russian project [45] of the Russian Federal Nuclear Center (Sarov) with the participation of IAP RAS. This project directly continues the research in [23]. In addition to the laser, which is similar to that used in Ref. [23], one more parametric amplifier was created on a DKDP crystal with the diameter 200 mm. The system was pumped by one of the channels of the Luch setup [46] (the energy of the second harmonic radiation pulse was 1 kJ and the duration was 2 ns). The master oscillator for the channel of the Luch setup was the specially designed laser, which provided the synchronization of the pump with both a femtosecond laser and a laser that pumped previous cascades of the parametric amplifier [47]. The maximum energy of a chirped pulse after the output cascade of the amplifier was about 100 J [45]. The efficiency of a four-grating compressor was 68%. It is assumed that the work on pulse compressing will be finished in 2008 – 2009 with the output power about 2 PW.

In 2011, it is planned to finish the construction of a 10-petawatt OPCPA laser at the Rutherford Laboratory (Great Britain) [24]. For pumping two final amplifiers, two channels of a Vulcano neodymium glass laser are used with the pulse energy 600 J each. Similarly to [23, 45], ultrawide phase matching is used in a DKDP crystal at the chirped pulse wavelength 910 nm. This project is special in that the chirped pulse is very long (3 ns).

Recently, two large Pan-European laser projects have started up: HiPER (High Power laser Energy Research) [48] and ELI (Extreme Light Infrastructure) [49]. The HiPER project is aimed at investigating laser fusion at a relatively moderate radiation energy that presses a laser target: less than 0.4 MJ for the second harmonic, in contrast to 1.8 MJ for the

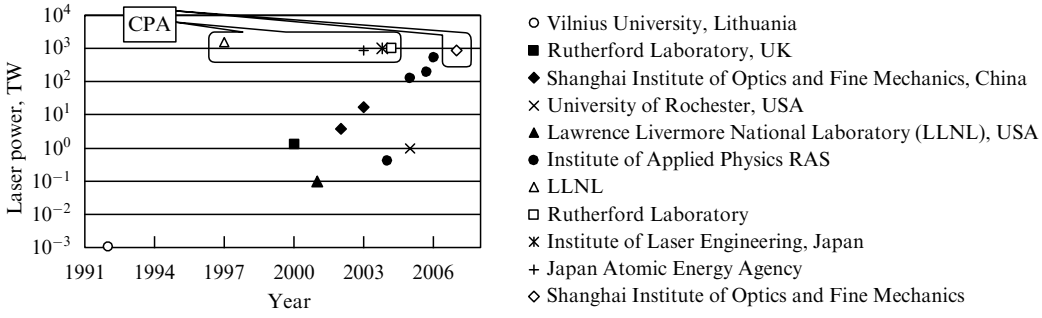

Figure 5. OPCPA lasers and petawatt CPA lasers.

third harmonic using the NIF (National Ignition Facility) setup [50]. Such energy 'saving' is reached due to the use of shorter pulses (of the order of 1 ps) with the energy from 150 to 2000 PW, in addition to nanosecond pulses, for igniting a thermonuclear target. The ELI project is aimed at the creation of a superhigh-power (50 – 1000 PW) femtosecond laser for carrying out unique scientific investigations. In these Pan-European projects, similarly to the project in [45], the architecture of a femtosecond laser used in [23] (parametric amplification of chirped laser pulses with the central wavelength 910 nm in a DKDP crystal) is considered optimal for further scaling.

The OPCPA design is not the only scheme intended for the future creation of multipetawatt and exawatt lasers. It is probable that sapphire crystals will be created with an aperture of 30 – 40 cm, or several types of neodymium glass will be used for expanding the gain spectral width. There is a very interesting concept concerning laser ceramics, a new optical material that combines the advantages of glass and single crystals. Laser ceramics has already made a substantial contribution to lasers with high average power [51]. There are numerous publications on femtosecond low-power ceramic lasers. In high-power lasers, ceramics has not been used in practice yet. However, ceramics-based lasers may compete with neodymium glass lasers, sapphire lasers, and OPCPA lasers.

In particular, a concept was suggested [52] for creating ultrahigh-power femtosecond lasers based on Cr:YAG ceramics, which combines the traditional principles (the energy source is nanosecond pulses of a neodymium glass laser, CPA) and new possibilities opened due to the use of laser ceramics. It can be seen from Table 1 that Cr:YAG ceramics has three key properties: a wide gain band, which provides amplification of pulses with the duration down to 20 fs; a large aperture, which allows amplifying chirped pulses to the multi-kilojoule level; and high conversion efficiency for the narrow-band radiation of a neodymium glass laser. These properties open up the possibility of creating a unique laser with the peak power 100 PW at the pumping energy 10 kJ. Although elements from Cr:YAG ceramics have not yet been used as active elements, they are widely used [53, 54] in passive Q-switches.

In addition to a wide aperture, a very important advantage of ceramics is the possibility of producing active media that cannot be grown as a single crystal. These are, for example, sesquioxides of rare earth elements doped with neodymium and ytterbium: Nd:Y_2O_3 [55], Nd:Lu_2O_3 [56], (Nd,Yb):Sc_2O_3 [57], Yb:Y_2O_3 [58], and so on. In Ref. [59], generation on Yb:Lu_2O_3 and Yb:Sc_2O_3 crystals was obtained with the respective durations 65 and 70 fs. This suggests one more variant for creating a multipetawatt laser: CPA in wide-aperture (Nd,Yb):Lu_2O_3 or (Nd,Yb):Sc_2O_3 ceramics pumped by flash lamps similar to neodymium glass lasers, which exhibit a substantially longer pulse duration. Excitation is transferred from neodymium ions to ytterbium ions, which provides a wide band (direct pumping of ytterbium is only possible by diode lasers, which hinders the possibilities of scaling). Even wider spectral bands can be obtained by using several oxide crystals (Sc_2O_3, Y_2O_3, Lu_2O_3, and so on) simultaneously, similarly to the case of the simultaneous use of different types of neodymium glasses [12, 50] or several garnets with chromium ions [52]. Thus, new petawatt and multipetawatt projects based on CPA in laser ceramics may arise in the immediate future.

6. Conclusion

Petawatt lasers created all over the world will soon become instruments for studying a new branch of knowledge, the physics of extreme light fields [49]. In the future, petawatt lasers may be used as accelerators of charged particles in fundamental investigations and in military, technological, and medical applications. Examples of the last one are isotope facilities for positron-emission tomography and compact, cheap sources of ions for hadronic therapy.

These and other potential applications, along with the noticeable progress in petawatt laser technology, interest commercial companies in expanding to the petawatt range, which accelerates laser technology development. It is hoped that in 5 – 10 years, petawatt lasers (including OPCPA lasers) will no longer be exotic and will become accessible in many laboratories throughout the world.

References

1. Strickland D, Mourou G *Opt. Commun.* **56** 219 (1985)
2. Pennington D M et al. *Proc. SPIE* **3047** 490 (1997)
3. Moulton P F *J. Opt. Soc. Am. B* **3** 125 (1986)
4. Aoyama M et al. *Opt. Lett.* **28** 1594 (2003)
5. Piskarskas A, Stabinis A, Yankauskas A *Usp. Fiz. Nauk* **150** 127 (1986) [*Sov. Phys. Usp.* **29** 869 (1986)]
6. Lozhkarev V et al., Preprint No. 720 (Nizhnii Novgorod: Inst. of Appl. Phys. of the Russ. Acad. of Sci., 2006)
7. Barty C P J et al., in *Proc. Conf. on Lasers and Electro-Optics* (*CLEO*): *San Francisco, Calif., May 17 – 21, 2004* (Washington, DC: Opt. Soc. of Am., 2004) p. JTuG4
8. Waxer L J et al. *Opt. Photon. News* **16** (7) 30 (2005)
9. Kitagawa Y et al. *IEEE J. Quantum Electron.* **40** 281 (2004)
10. Danson C N et al. *Nucl. Fusion* **44** S239 (2004)
11. Blanchot N et al. *Proc. SPIE* **5975** 59750C (2005)
12. Gaul E et al., in *Proc. Advanced Solid-State Photonics, Nara, Japan, January 27 – 30, 2008*, p. MC3
13. Zhu Q et al. *Proc. SPIE* **6823** 682306 (2007)
14. Perry M D et al. *Opt. Lett.* **24** 160 (1999)
15. Collier J L et al., in *Proc. Conf. on Lasers and Electro-Optics* (*CLEO*): *Baltimore, MD, May 22 – 27, 2005* (Washington, DC: Opt. Soc. of Am., 2005) p. JFB1
16. Liang X et al. *Opt. Express* **15** 15335 (2007)
17. Yanovsky V et al. *Opt. Express* **16** 2109 (2008)
18. Ross I N et al. *J. Opt. Soc. Am. B* **19** 2945 (2002)
19. Yang X et al. *Opt. Lett.* **27** 1135 (2002)
20. Andreev N F et al. *Pis'ma Zh. Eksp. Teor. Fiz.* **79** 178 (2004) [*JETP Lett.* **79** 144 (2004)]
21. Lozhkarev V V et al. *Pis'ma Zh. Eksp. Teor. Fiz.* **82** 196 (2005) [*JETP Lett.* **82** 178 (2005)]
22. Lozhkarev V V et al. *Opt. Express* **14** 446 (2006)
23. Lozhkarev V V et al. *Laser Phys. Lett.* **4** 421 (2007)
24. Chekhlov O et al. *Proc. SPIE* **6735** 67350J (2007)
25. Karsch S et al., in *Proc. Advanced Solid-State Photonics, Nara, Japan, January 27 – 30, 2008*, p. WF1
26. Butkus R et al. *Appl. Phys. B* **79** 693 (2004)
27. Lozhkarev V V et al. *Laser Phys.* **15** 1319 (2005)
28. Ross I N et al. *Opt. Commun.* **144** 125 (1997)
29. Matousek P, Rus B, Ross I N *IEEE J. Quantum Electron.* **36** 158 (2000)
30. Ross I N et al. *Appl. Opt.* **39** 2422 (2000)
31. Chekhlov O V et al. *Opt. Lett.* **31** 3665 (2006)
32. Freidman G I et al. *Proc. SPIE* **4630** 135 (2002)
33. Freidman G et al. *Proc. SPIE* **4972** 90 (2003)
34. Yanovsky V et al. *Opt. Lett.* **18** 1541 (1993)
35. Ivanov A A, Alfimov M V, Zheltikov A M *Laser Phys.* **10** 796 (2000)
36. Yakovlev I V et al. *Proc. SPIE* **6614** 661403 (2007)
37. Freidman G I, Yakovlev I V *Kvantovaya Elektron.* **37** 147 (2007) [*Quantum Electron.* **37** 147 (2007)]

38. Potemkin A K et al. *Kvantovaya Elektron*. **35** 302 (2005) [*Quantum Electron*. **35** 302 (2005)]
39. Katin E V, Lozhkarev V V, Palashov O V, Khazanov E A *Kvantovaya Elektron*. **33** 836 (2003) [*Quantum Electron*. **33** 836 (2003)]
40. Poteomkin A K et al. *IEEE J. Quantum Electron*. (to be published)
41. Potemkin A K et al. *Appl. Opt*. **46** 4423 (2007)
42. Martyanov M A, Poteomkin A K, Shaykin A A, Khazanov E A *Kvantovaya Elektron*. **38** 354 (2008) [*Quantum Electron*. **38** 357 (2008)]
43. Vlasov S N, Talanov V I *Samofokusirovka Voln* (Self-focusing of Waves) (Nizhny Novgorod: Inst. Prikladnoi Fiziki RAN, 1997)
44. Khazanov E A et al., in *Proc. Conf. on Lasers and Electro-Optics* (*CLEO*): *San Jose, CA, 2008* (Washington, DC: Opt. Soc. of Am., 2008) p. CThX6
45. Belov I A et al., in *Trudy Mezhdunar. Konf. X Kharitonovskie Tematicheskie Chteniya, 11–14 Marta 2008 g., Sarov* (Proc. of Intern. Conf. X Kharitonov Topical Readings, 11 – 14 March 2008, Sarov) (Sarov: RFYaTs – VNIIEF, 2008) p. 145
46. Garanin S G et al. *Kvantovaya Elektron*. **35** 299 (2005) [*Quantum Electron*. **35** 299 (2005)]
47. Palashov O V, Katin E V, Luchinin G A, Khazanov E A *Appl. Opt*. **47** 3124 (2008)
48. HiPER, http://www.hiper-laser.org/
49. ELI: the Extreme Light Infrastructure european project, http://www.extreme-light-infrastructure.eu/
50. Miller G H, Moses E I, Wuest C R *Nucl. Fusion* **44** S228 (2004)
51. Yamamoto R M et al., in *Proc. Advanced Solid-State Photonics, Nara, Japan, January 27 – 30, 2008*, p. WC5
52. Khazanov E A, Sergeev A M *Laser Phys*. **17** 1398 (2007)
53. Takaichi K et al. *Jpn. J. Appl. Phys*. **41** L96 (2002)
54. Feng Y et al. *Appl. Opt*. **43** 2944 (2004)
55. Lupei A et al. *J. Luminescence* **102 – 103** 72 (2003)
56. Lu J et al. *Appl. Phys. Lett*. **81** 4324 (2002)
57. Lupei V, Lupei A, Ikesue A, in *Proc. Conf. on Lasers and Electro-Optics* (*CLEO*): *San Francisco, Calif., May 17 – 21, 2004* (Washington, DC: Opt. Soc. of Am., 2004) p. CThT55
58. Shirakawa A et al. *Opt. Express* **11** 2911 (2003)
59. Tokurakawa M et al. in *Proc. Advanced Solid-State Photonics, Nara, Japan, January 27 – 30, 2008*, p. WB16